2017

KaSI: a Ka-band and S-band Cross-track Interferometer

Gerard Ruiz Carregal
University of Massachusetts Amherst

KASI: A KA-BAND AND S-BAND CROSS-TRACK INTERFEROMETER

A Thesis Presented

by

GERARD RUIZ CARREGAL

Submitted to the Graduate School of the
University of Massachusetts Amherst in partial fulfillment
of the requirements for the degree of

MASTER OF SCIENCE IN ELECTRICAL AND COMPUTER ENGINEERING

February 2017

Electrical and Computer Engineering

KASI: A KA-BAND AND S-BAND CROSS-TRACK INTERFEROMETER

A Thesis Presented

by

GERARD RUIZ CARREGAL

Approved as to style and content by:

Paul Siqueira, Chair

Robert W. Jackson, Member

Patrick A. Kelly, Member

C.V. Hollot, Department Head
Electrical and Computer Engineering

DEDICATION

To my parents.

ACKNOWLEDGMENTS

First of all, I would like to thank my advisor, Paul Siqueira, for giving me this opportunity. Paul, your support, help and lessons made this work possible. Thanks also to professors Robert W. Jackson and Patrick A. Kelly for being part of my committee and taking the time to read this thesis. For the last three years I had the chance to work with amazing people that contributed in this project. I would like to thank Dustin for all his help, this work is also yours. Thanks to Tom, Chen, Tracy, Sheila, Krzysztof, Kan and Yang for helping me with the radar testing and giving ideas. Katerina, Gerard, John, Ruben, Miguel and Jezabel, Amherst would not have been the same place without all of you. Living far away from home would have been much harder without your unconditional support and encouragement, thank you, Aina. Finally, I would like to thank my parents who always believe in me and support me in any decisions I make, this work is dedicated to both of you.

ABSTRACT

KASI: A KA-BAND AND S-BAND CROSS-TRACK INTERFEROMETER

FEBRUARY 2017

GERARD RUIZ CARREGAL

B.S., POLYTECHNIC UNIVERSITY OF CATALONIA

M.S.E.C.E., UNIVERSITY OF MASSACHUSETTS AMHERST

Directed by: Professor Paul Siqueira

A dual-frequency system is needed to better understand natural processes that constitute the environment and seasonal cycles of the Earth. A system working at two different wavelengths acquiring data simultaneously will give a valuable dataset since the conditions on the ground will be exactly the same. Hence, elements such as wind, soil moisture or any other changes on the ground will not interfere in the measurements. This thesis explains how an S-band radar was built and tested. Moreover, the experiments done with a Ka-band radar used as a scatterometer are explained as well as the data processing and analysis. Finally, the two systems are used to get dual-frequency measurements from an airborne platform. The dual-frequency data is explored, showing the differences in normalized radar cross-section between frequencies and discussing the interferometric measurements.

TABLE OF CONTENTS

LIST OF TABLES

Table **Page**

LIST OF FIGURES

Figure **Page**

CHAPTER 1

INTRODUCTION AND MOTIVATION

This thesis presents three different instruments: an S-band synthetic aperture radar(SAR), a Ka-band scatterometer and a dual-frequency interferometric SAR. The work done, the motivation and the goals are different for each system. The S-band radar has been designed, built, tested and deployed from scratch. The Ka-band scatterometer presented in this work was built using most of the work done on the Ka-band radar developed at MIRSL [7][10]. The research discussed here is focused on improving the system to collect science data and processing. Regarding the dual-frequency system, the thesis describes the first steps taken to build an S-band and a Ka-band dual-frequency InSAR system that could potentially be used for tree height estimation or snow depth measurements.

Two different radar spaceborne missions, NISAR and SWOT, are currently being developed by space agencies and will be used for Earth observation. The instruments presented in this thesis have the potential to be used in support of both missions.

1.1 NISAR and the S-band radar

There is a pressing need in the scientific community for new data that allow the study of highly spatial and complex processes occurring on the Earth. For instance, the study of ecosystems, ice dynamics or solid earth geophysics need new instruments capable of acquiring data with high coverage in space and time. The NASA-ISRO Synthetic Aperture Radar (NISAR) mission will acquire radar images globally, providing scientists with these valuable datasets.

The NISAR mission is a joint effort between the National Aeronautics and Space Administration (NASA) and the Indian Space Research Organization (ISRO). The mission will launch a satellite equipped with two Synthetic Aperture Radar (SAR) systems working at L-band and S-band. NISAR will provide the necessary measurements that will be decisive in the study of ecosystem disturbances or natural hazards. The obtained data will help the scientific community to study ecosystems (biomass, effects of changing climate on habitats and CO2, agriculture), ice dynamics (ice velocity and thickness, response of ice sheets to climate change and sea level rise) and solid earth geophysics (surface deformation, hazards response and water resource management). The research in these fields will improve, for instance, disaster forecasting (earthquakes, volcanoes, floods...) or the understanding of how the climate change affects the carbon cycle [2].

The S-band radar described in this thesis has the potential to help to characterize the response of the radar for different targets, explore interferometry at this band and validate the data algorithms used by the NISAR satellite.

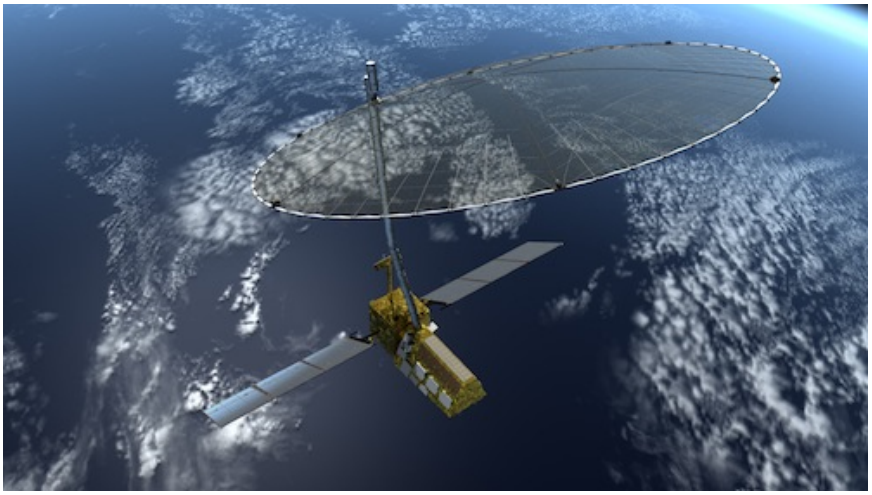

Figure 1.1: NISAR mission satellite concept.

1.2 SWOT and the Ka-band scatterometer

The study of oceans and inland water bodies is fundamental to understanding the global water cycle, the weather, and climate change. These are complex processes that need instruments capable of measuring water storage changes in wetlands, reservoirs and lakes as well as global measurements of ocean surface topography at finer resolutions than the currently available. The Surface Water & Ocean Topography (SWOT) mission, an international mission between NASA, France and other partners, plans to measure these processes at finer scales than current altimeter missions.

The SWOT mission will focus on oceanographic and hydrologic measurements. The main oceanographic objective of the SWOT mission is to characterize short scale dynamics of ocean variability, the ocean mesoscale and submesoscale circulation processes [8]. Regarding hydrologic measurements, SWOT's main objectives include characterizing the spatial and temporal variations in surface waters. Furthermore, the mission will study coastal ocean dynamics, coastal tides and internal tides, terrestrial water cycle, floodplains and wetlands.

The SWOT mission's main instrument is a Ka-band Radar Interferometer (KaRIN). Unlike conventional profile altimeters, KaRIN will have a swath with look angles smaller than 4°. As it can be seen in Figure 1.2, KaRIN will use two antennas to perform interferometric measurements. The Ka-band radar developed at MIRSL [7], with similar frequency and bandwidth specifications as KaRIN, has the potential to support the SWOT mission. This thesis describes the work done to measure the radar backscatter using the Ka-band radar adapted to a nadir-looking geometry.

1.3 Dual frequency system

The dual-frequency radar is motivated by the need of new instruments to better understand natural processes that constitute the environment and seasonal cycles of the Earth. A dual-frequency radar can be used to explore the ability to better measure

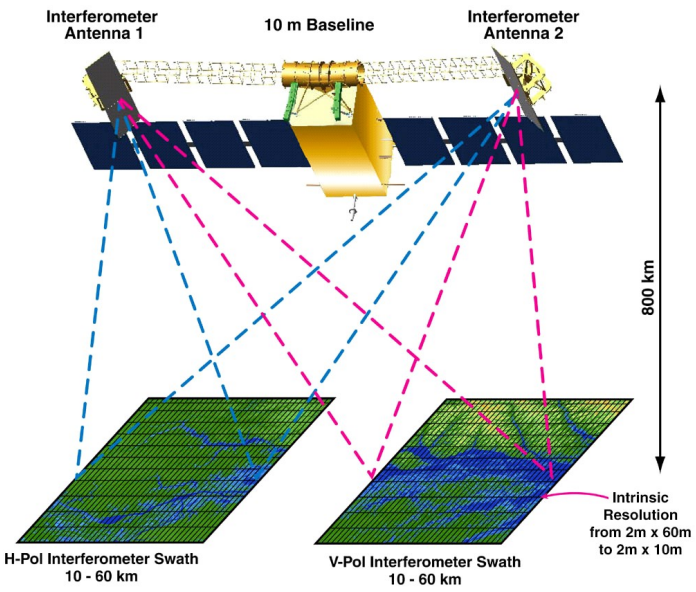

Figure 1.2: SWOT mission: KaRIN system setup. Two antennas will be used, each one with two footprints.

and estimate, for instance, snow parameters such as grain size or snow layer depth [6]. The NISAR and SWOT missions will have S-band, L-band and Ka-band radars on board. This opens the possibility of combining the data of the two missions. The work on the dual-frequency radar presented here will help to explore some of the data products that might be obtained and has the potential to help in the development of future algorithms.

1.4 Summary of chapters

The thesis is mainly organized in four blocks: radar concepts, S-band radar, Ka-band radar and a dual-frequency radar. Chapter 2 covers the basic radar theory, focusing on pulse compression, synthetic aperture radar (SAR) and interferometry. Chapter 3 describes the S-band system design: radar transceiver, acquisition system, supporting electronics, as well as the ground tests and flight measurements. Chapter 4 focuses on the Ka-band radar used as a scatterometer, with special emphasis on the data processing and the obtained results. The last block, Chapter 5, describes

the work done on merging the S-band and Ka-band radars into the dual-frequency system and discusses the first results, showing the differences in radar cross-section between frequencies and analyzing the first interferograms.

CHAPTER 2

RADAR CONCEPTS

Traditional pulsed radar transmits a pulse and waits for the echoes, or backscattered pulses. The echoes are downconverted to baseband and sampled. Then, a matched filter is applied to range compress the pulses. The pulsed radar system requires high sampling rates that generate big amounts of data. A different approach is used in Frequency Modulated Continuous Wave (FMCW) radar, where the system transmits and receives simultaneously. The pulse used is a linear frequency modulated pulse or linear chirp. The transmitted signal is used as an oscillator and mixed with the received signal. Thus, FMCW implements the matched filtering in hardware using a mixing operation. Each one of the systems have advantages and disadvantages over the other. FMCW allows lower sampling and data rates. Also, less power is needed compared to a pulsed radar. However, FMCW radar uses two antennas, one for transmit and the other for receive, while a pulsed radar only needs one. The coupling between antennas and the consequent saturation of the receiver chain is a common issue in FMCW radar that usually limits the performance of the system.

2.1 FMCW radar basics

As mentioned previously, FMCW radar uses a linear chirp that changes its frequency linearly with time. The time-domain expression for the pulse is given by

$$x_t(t) = cos(2\pi f_0 t + \pi\beta t^2 + \phi_0), \tag{2.1}$$

where β is the chirp rate

$$\beta = \frac{B}{\tau}. \tag{2.2}$$

B is the bandwidth of the pulse and τ the sweep time. The instantaneous frequency can be derived as

$$f_{t_i} = \frac{1}{2\pi}\frac{d}{dt}(2\pi f_0 t + \pi\beta t^2 + \phi_0) = f_0 + \beta t. \tag{2.3}$$

Figure 2.1 shows the linear slope of the chirp's frequency. As it will be shown later, the linearity of the chirp is used to map to the range domain.

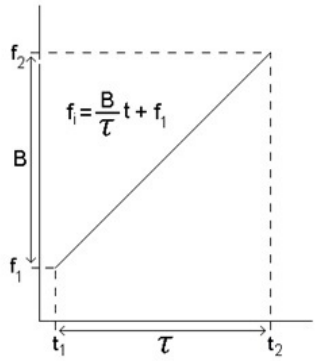

Figure 2.1: Linear chirp. Time is the x-axis and frequency the y-axis. The chirp presents a linear relationship between time and frequency.

The transmitted pulse is backscattered and received as

$$x_r(t) = x_t(t - \tau_0) = cos(2\pi f_0(t - \tau_0) + \pi\beta(t - \tau_0)^2 + \phi_0), \tag{2.4}$$

where

$$\tau_0 = \frac{2R}{c} \tag{2.5}$$

is the delay or time of flight. Here, R is the range to the target and c is the speed of light. For simplicity, in this model, the amplitude of the received signal has not been taken into account.

The pulse compression for an FMCW radar is done in hardware using a mixer and a low-pass filter. The transmit pulse is used as the Local Oscillator (LO) in the mixer. The mixing operation yields a tone which is proportional to the delay between the transmit and receive pulses and to the chirp rate. β. The mixing and filtering operations will result in the following expression:

$$x_c(t) = x_t(t) \cdot x_r(t) = \frac{1}{2} cos(2\pi f_0 \tau_0 - \pi\beta\tau_0^2 + 2\pi\beta t\tau_0). \tag{2.6}$$

The instantaneous frequency of the pulse compressed signal, $x_c(t)$ is

$$f_{c_i}(t) = \frac{1}{2\pi}\frac{d}{dt}(2\pi f_0\tau_0 - \pi\beta\tau_0^2 + 2\pi\beta t\tau_0) = \beta\tau_0, \tag{2.7}$$

which is also known as the beat frequency, f_b and can be expressed as

$$f_b = \beta\tau_0 = \frac{B}{\tau}\tau_0, \tag{2.8}$$

It is easy to see that the resulting tone is proportional to the linear slope of the chirp, β, and the time delay between the transmit pulse and the received pulse, τ_0. Substituting Equation (2.5) in Equation (2.8) yields

$$f_b = \frac{B}{\tau}\frac{2R}{c}, \tag{2.9}$$

which can be rewritten as

$$R = \frac{cf_b\tau}{2B}. \tag{2.10}$$

Note that there is a linear mapping between range and frequency. Thus, the pulse compression done by hardware gives an expression that directly relates range with frequency. A Fast Fourier Transform (FFT) applied to the time-domain sampled

signal is used to get the range compressed signal, allowing mapping frequency to range.

It is worth analyzing Equation (2.9) and its parameters. While the speed of the light, c, is a constant, the rest of parameters are system and/or experiment dependent. Assuming the bandwidth and the sweep time are fixed for all deployments, the range is left as a variable. The maximum range of the system will ultimately be determined by the sampling frequency of the system. Hence, the maximum range is

$$R_{max} = \frac{c f_{max} \tau}{2B}, \tag{2.11}$$

where the maximum frequency depends on the sampling frequency which is chosen based on the Nyquist criteria. Thus,

$$f_{max} = \frac{f_s}{2}. \tag{2.12}$$

The maximum range, the furthest the radar can receive backscattered pulses, will depend on the altitude of the system, look angle, transmit power, receiver sensibility and other parameters. Therefore, the sampling frequency depends on each of the experiment setups and objectives.

A radar will resolve a point target in two directions: cross-track and along track. The cross-track or range direction is perpendicular to the moving direction of the platform. The along-track or azimuth direction is perpendicular to the cross-track. The resolution on each dimension will depend on different parameters of the system. The range resolution depends on the speed of light and the bandwidth of the pulse:

$$\Delta r = \frac{c}{2B}. \tag{2.13}$$

The azimuth resolution is proportional to the azimuth beamwidth of the antenna and the range to the target:

$$\Delta az = R \cdot \theta_{az_{3dB}}. \tag{2.14}$$

Therefore, the range resolution is constant at any range while the azimuth resolution worsens with range. SAR processing can be used to improve the azimuth resolution as it will be shown in the next section.

2.2 Synthetic Aperture Radar

Synthetic Aperture Radar is a radar system that uses a processing technique that improves the azimuth radar resolution. The principle of the technique is to take advantage of the platform's motion where the radar is mounted to synthesize an antenna array. Theoretically, the azimuth resolution achieved with SAR processing is half of the antenna length:

$$\Delta az_{SAR} = \frac{L}{2}, \tag{2.15}$$

where L is the length of the antenna. Note that in this expression the resolution does not depend on the range to the target.

There are two approaches to processing the data: time domain and frequency domain. The time domain algorithm is simple and implicitly compensates for motion of the platform. Knowing the precise imaging geometry is required for the algorithm to work, which might be the biggest disadvantage of this method. Therefore, good GPS and Inertial Motion Unit (IMU) data is needed, as well as using a Digital Elevation Model (DEM). On the other hand, the frequency domain algorithms are usually more complex and the motion compensation needs to be addressed as a separate problem. However, these algorithms have the advantage of being less computationally intense which make them suitable for larger datasets.

The results presented in this thesis are based on the time domain backprojection algorithm [3]. Essentially, the backprojection algorithm coherently adds all of the

pulses contributing to a certain target. Thus, a matched filter is applied to the range compressed received signal to compensate for the phase due to the round-trip travel of the pulse from the transmit antenna to the phase-center of the scattering-cell and back to the receive antenna.

The simplified exponential form for the pulse compressed received signal can be written as

$$x_{comp}(t,n) = A \cdot exp(-jkd_n), \tag{2.16}$$

where n is the slow-time index, the time associated with the pulse repetition frequency; t is the fast-time index, which is related to the distance traveled by the pulse from the antenna to the target at the speed of light; A is an amplitude term, k the wavenumber and d_n the distance to the phase-center of the scattering-cell (i.e., physical center of the phase). Thus, the matched filter for azimuth compression can be written as

$$h_{az}(t,n) = exp(-jk\tilde{d}_n). \tag{2.17}$$

Here, $\tilde{d}_n$ is the distance to the center of the resolution-cell. Note that while our estimation $\tilde{d}_n$ is similar to d_n in most of the cases, they are not usually the same. A worst case scenario, where the difference between d_n and $\tilde{d}_n$ is maximized, would be having a point scatterer on one of the corners of the resolution-cell. The physical phase-center would be situated in the corner but the matched filter would still use the center of the resolution-cell. This difference results in a residual phase that is exploited in interferometry to estimate the height of the targets.

The backprojected pixel value is the coherent sum of all the pulses contributing to the scattering-cell. Therefore, applying the matched filter and summing gives

$$I = \sum_{n \in N} x_{comp}(t,n) \cdot \overline{h_{az}(t,n)} = \sum_{n \in N} A \cdot exp(-jkd_n) \cdot exp(jk\tilde{d}_n) = \sum_{n \in N} A \cdot exp(jk\Delta d_n). \tag{2.18}$$

In this expression, I is the backprojected pixel value, N is the set of all pulses contributing to the scattering-cell and Δd_n is the difference between d_n and $\tilde{d}_n$,

$$\Delta d_n = \tilde{d}_n - d_n. \tag{2.19}$$

This operation is applied to every pixel of the image to form the SAR processed image. A detailed derivation of the algorithm can be found in [3] and [5].

2.3 Interferometry

Interferometry is a technique used to resolve a target's third dimension: height. As explained in previous sections, by using one antenna, a radar can resolve a target in two dimensions: range and azimuth. Observing the same target from slightly different spatial positions and by using trigonometry, the remaining third dimension of a target can be inferred. Two different methods can be used to observe the same target from different spatial positions: repeat-pass and single-pass interferometry. In repeat-pass interferometry, the platform observes the same targets flying an approximate flight path in temporally spaced acquisitions. Single-pass interferometry uses two spaced receive antennas mounted on the moving platform. The system presented in this thesis is based on single-pass interferometry.

The interferometric mathematical model used to infer height depends on the SAR processing applied to the raw data and hence, the approach to get interferograms differs between frequency-domain and time-domain SAR processing. As mentioned in the previous section, the time-domain backprojection algorithm is mainly used to process the data presented here. Therefore, the interferometric model discussed in the next lines is based on the backprojection algorithm.

The geometry for a single-pass interferometric radar is shown in Figure 2.2. The dots in this figure represented by A and B denote the two receive antennas. The

separation between the antennas is called the baseline. The center of resolution-cell is denoted by C. The estimated distance from each of the antennas to C is $\tilde{d}$. The phase-center of the scattering-cell for each of the antennas is denoted by D and E. Finally, d is the distance from each of the antennas to the phase-center of the scattering-cell. Recall that, by applying the time-domain backprojection algorithm, the phase is proportional to the difference between $\tilde{d}$ and d. Therefore, the phase of each receiver is determined by this difference.

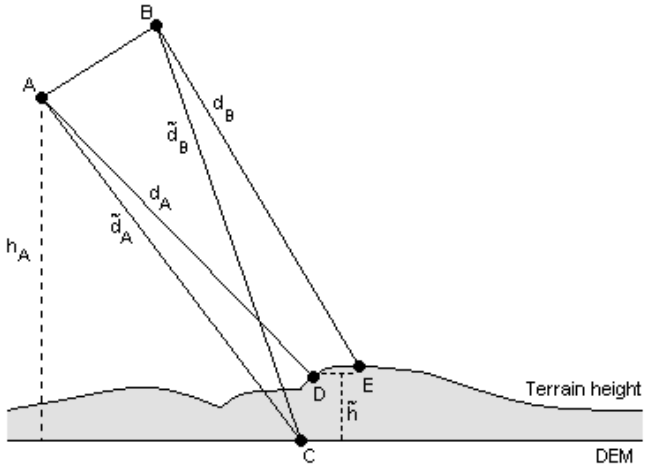

Figure 2.2: Single-pass time-domain interferometry geometry.

The difference in phase between two channels is calculated using the correlation,

$$\rho_{A,B} = \frac{E[x_A x_B^*]}{\sqrt{E[|x_A|^2]}\sqrt{E[|x_B|^2]}}, \tag{2.20}$$

where x_A and x_B correspond to complex zero-mean random variables associated with the pixels of each channel. The magnitude of the correlation gives information on the quality of the data. The noise is uncorrelated and thus, a low correlated magnitude will not provide reliable phase information since it is dominated by noise. The phase of the correlation is the difference of phase between the two channels.

The time-domain backprojection interferometric phase difference is given by

$$\Delta\Phi = k(\Delta d_A - \Delta d_B), \tag{2.21}$$

where k is the wavenumber and Δd is the difference of distances shown in Equation (2.19), derived from the SAR processing described in Section 2.2. Here, the subindices A and B correspond to each of the receive antennas. As it can be seen in Figure 2.2, since the two receive antennas observe the resolution-cell from slightly different angles, the phase-center of the scattering-cell is not the same for each receiver, hence Δd_A and Δd_B are different. Starting with the displacement between phase-centers and through further assumptions and derivations, the height of the target can be estimated as

$$\tilde{h} = \frac{\Delta\Phi \tilde{d_A} \tilde{d_B}}{k(\tilde{d_B}(h_A - h_C) - \tilde{d_A}(h_B - h_C))}, \tag{2.22}$$

where $\Delta\Phi$ is the measured phase obtained from the correlation, $\tilde{d}_A$ and $\tilde{d}_B$ are the estimated distances to the phase-center (i.e., the distance to the center of the resolution-cell), h_A and h_B the altitude of the two receive antennas and h_C the estimated height of the phase-center of the target observed (obtained from a DEM).

The reader should refer to [3] for the detailed mathematical derivation and analysis.

CHAPTER 3

S-BAND RADAR

The S-band radar discussed in this thesis has been in continuous development at MIRSL since November 2013. The following sections describe how it was designed, mounted and tested during fall 2013 and spring 2014 as well as most recent improvements.

3.1 System design

3.1.1 System overview

The S-band radar system is composed of the radar transceiver, with a transmit antenna and two receivers; a signal generator, the power supply, that includes a GPS receiver and a 10 MHz local oscillator and the acquisition system.

The signal generator generates a chirp pulse with a pulse repetition frequency (PRF) of 999 Hz and a trigger interval of 1.001 ms. Every time a new pulse is generated, the TTL rising pulse (trigger) is sent to the Analog to Digital Converter (ADC). Once the chirp signal is generated, it enters into the transceiver. The transceiver also gets a 10 MHz reference signal that is used to phase lock the local oscillators. The chirp signal coming from the signal generator is split. One of the split signals travels through the up-converter and it is transmitted. The other is used as oscillator in the signal compression stage. The echo is received in both receive antennas and it is down-converted. The signal compression stage is applied to both receive channels to perform chirp compression in real time. Finally, the ADC will sample the signal of the receive channels and write the samples into a file.

The signal generator is the Tektronix AFG3252 and the acquisition system is the Ettus Research USRP N210. The power supply and the antenna will be briefly described in the following sections.

3.1.2 Power supply

Initially, the power supply used for the system was adopted from a previous instrument (TIMMi) with some minor modifications. To reduce the dimensions of the system a new power supply enclosure was built with the following elements:

- VI-RAM-E1. Ripple Attenuator Module (RAM) used to attenuate the spurs introduced by the 15 V power supply.
- VI-PUL2-IUX. This power supply has two outputs: 28 V and 15 V. The 28 V output is used for the High Power Amplifier (HPA) and for a 12 V DC to DC converter. The 15 V output is filtered by the RAM since it has shown to introduce spurs in the system. It is used to drive some of the amplifiers of the transceiver and the 10 MHz Local Oscillator (LO).
- 5EB150. Acopian 5 V power supply used for some of the transceiver amplifiers.
- Thales A12/AC12 GPS sensor. Another 15 V power supply is used to power this GPS.

3.1.3 Acquisition system, GPS and IMU

Two acquisition systems have been used. For the first flights, an NI PXIe-1062Q computer was used with an NI PXI-5152 8-bit 2 GS/s digitizer card. The computer added significant weight to the whole system and the performance was poor. To reduce the system weight and improve the system flexibility, an Ettus Research USRP N210 with a laptop was used for the next flights. This acquisition system is still under development and the following lines describes the system at the time of writing.

Each time a new data file is started, the time of the Ettus board is set using the pulse per second (PPS) trigger from the GPS as well as the GPS serial messages. The signal generator is used to trigger the Ettus board at every pulse. The data is written into a solid state drive. The maximum data rate is 50 MSPS (25 MSPS per channel, for two channels).

A Trimble Ag132 GPS and a DMS-EGP02 IMU are used to record position (latitude, longitude, altitude) and platform motion angles (pitch, roll and yaw). The data is saved into a file using the laptop.

3.1.4 Antennas

The system uses three antennas. One for the transmitter and two for the receivers. The antennas were designed and built at MIRSL, using a milling machine. The design is a six-patch array antenna with vertical and horizontal polarizations. The two polarization parameters have small differences, especially in the beamwidth of the antenna main-lobe in the azimuth and elevation directions. The center frequency is 3.2 GHz and the bandwidth 100 MHz. The azimuth beamwidth θ_H is 12 degrees (0.21 rad); the elevation beamwidth θ_V is 60 degrees; the gain in the main lobe is 12 dB; and the difference between the main lobe gain and the side lobe gain, the Side Lobe Level (SLL) is estimated to be 10 dB.

3.1.5 Aircraft door

The antennas were mounted at a fixed angle. The angle was chosen to be 45 degrees to illuminate well the far range of the swath while maintaining sufficient gain in the near range to achieve a good signal to noise ratio throughout. In short, the elevation beamwidth is wide enough to cover all possible look angles if the antennas are fixes at 45 degrees. The distance between the antennas was determined by taking the dimensions of the door and the response of the antennas into account. Since the main challenge has been to minimize the near field coupling between the transmitter

and the receivers, the distance between he transmit and receive antennas should be maximized. Figure 3.1 shows the setup that was used for the first construction of the S-band interferometer.

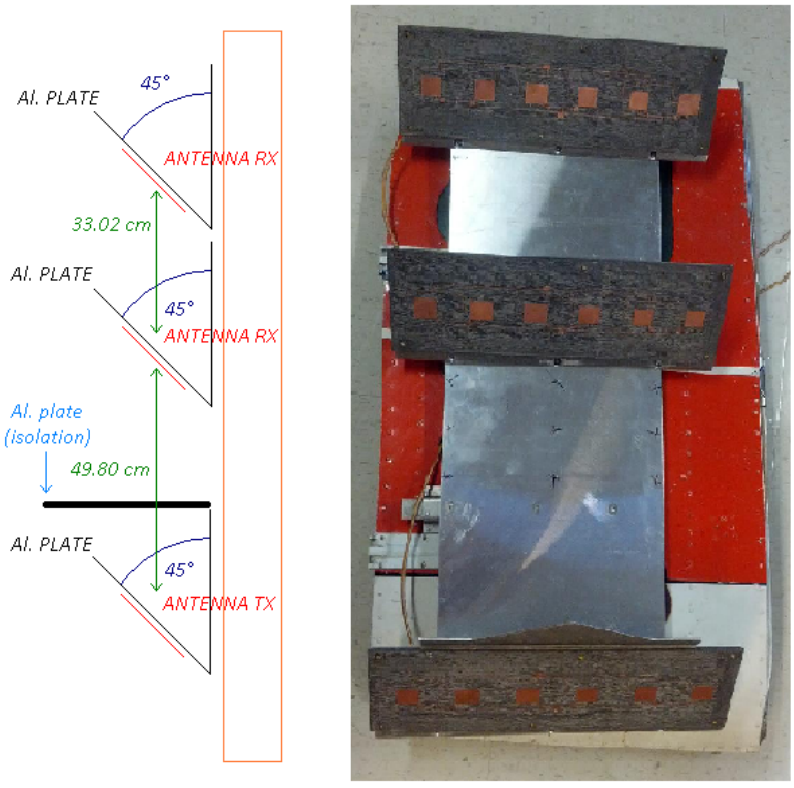

Figure 3.1: Sketch of the disposition of the antennas in the door and picture of the built structure.

3.1.6 Transciever overview

The radar uses two stages to convert the signal from base band to S-band. There are two reasons to use this design: image rejection improvement and the possibility to use an already existing L-Band PCB design in the future. Therefore, the radar has two up-conversion and two down-conversion stages. Moreover, since the radar will be used as a Frequency Modulated Continuous Wave (FMCW) system, a signal compression stage follows the receiver down-conversion. A stage for generating local

oscillators is also needed to perform the up-conversion and down-conversion. The block diagram is shown in Figure 3.2. The actual radar has two down-converters and two signal compression stages, one for each receive antenna. The phase of the signal received is important to generate interferometric images. Thus, the receivers should be as symmetric as possible to avoid different phase changes on each receiver. The mixer operations in the up-converter produce the sum and the difference of the two input and LO frequencies. Hence, there will be an upper sideband (sum) and a lower sideband (difference). In the system, the lower sideband is used in both up-conversions. In the down-converter, the mixing operations can result in false target detection if there is a strong signal in the image frequency band. The down-converter must be robust to the three image frequency bands that can be seen in Figure 3.3. The frequency specifications of the radar are listed in Table 3.1.

Parameter	**Value**
Maximum signal bandwidth	200 MHz
Used signal bandwidth	100 MHz
S-band center frequency	3.2 GHz
L-band center frequency	1.16 GHz
Base band center frequency	140 MHz
S-band LO frequency	4.36 GHz
L-band LO frequency	1.3 GHz

Table 3.1: Frequency specifications of the S-band radar.

3.1.7 Local oscillators stage

The transceiver requires three local oscillators for operation. These are 1.) at L-band (1.3 GHz), 2.) S-band (4.36 GHz) and 3.) for signal compression. The chirp pulse is split before it is sent to the up-converter, and used for mixing the received signal at baseband. The LOs are phase-locked by a 10 MHz sinusoidal signal provided externally. In Figure 3.4 the block diagram of this stage is shown.

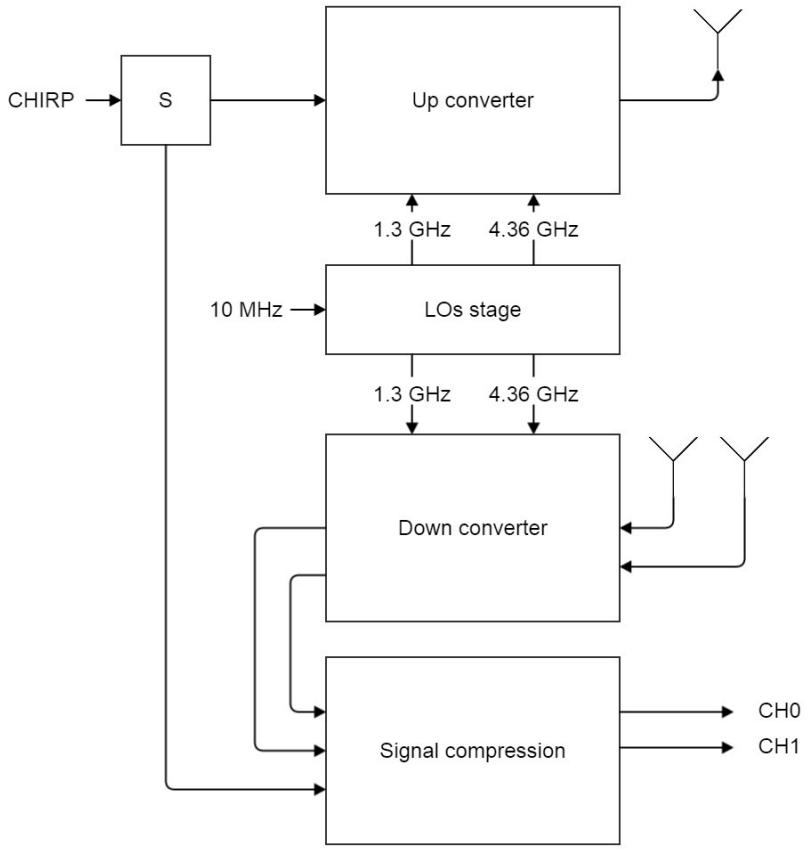

Figure 3.2: Block diagram of the transceiver of the radar.

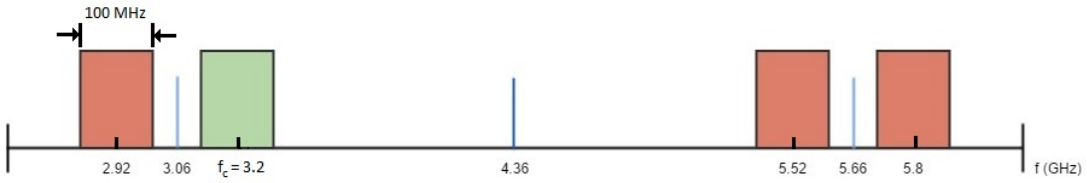

Figure 3.3: Spectrum with the three image frequency bands, in red; the local oscillators, in blue; and the working band of the radar, in green.

The components are listed in Table 3.2. The LOs are prototype boards, inexpensive compared to other LO. The frequency and the power can be modified using a computer and normally need to be set up every time through a USB connection when the boards are powered up. For this application, an Arduino board is used to set up

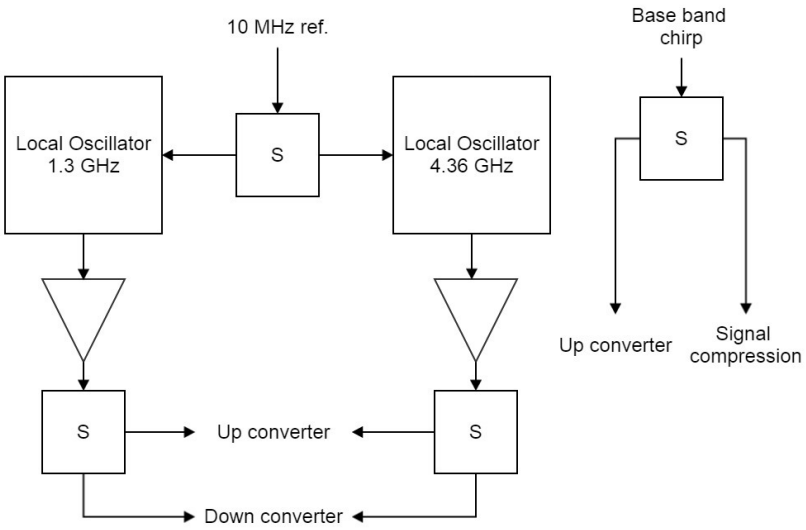

Figure 3.4: Block diagram of the local oscillators stage.

the registers of each prototype board automatically. The LOs have several harmonics that are attenuated by the amplifiers and splitters. Two splitters are used to bring the chirp signal to the up-converter and to the two signal compression stages. Two additional splitters for each LO are used to bring their signal to the up-converter and both down-converters.

3.1.8 Up-converter

Once the baseband signal enters into the up-converter, it is up-converted from baseband to L-band. A second stage up-converts it from L-band to S-band. Figure 3.5 shows the block diagram of the up-converter. Each sub stage of the up-converter is composed of a mixer that shifts up the signal in frequency. A filter follows that and attenuates the image frequency band as well as other harmonics and intermodulation products. Once at the center frequency (3.2 GHz), the signal is amplified by the High Power Amplifier (HPA).

Component type	Specifications	Use
Frequency Synthesizer with VCO (Eval. Board)	Band = 137.5-4400 MHz	Local oscillator at 1.3GHz and at 4.36GHz
Power Splitter	Insertion Loss 3.3dB	10 MHz reference signal splitting
Power Splitter	Insertion Loss 3.3dB	Chirp pulse splitting
Power Splitter	Insertion Loss 3.8dB	1.3 GHz splitting
Power Splitter	Insertion Loss 3.2dB	4.36 GHz splitting
Amplifier	Gain 12.8dB, P1=16dB	1.3 GHz amplifier
Amplifier	Gain 13dB, P1=17.5dB	4.36 GHz amplifier

Table 3.2: Components used in building the local oscillators stage. All of them have SMA connectors.

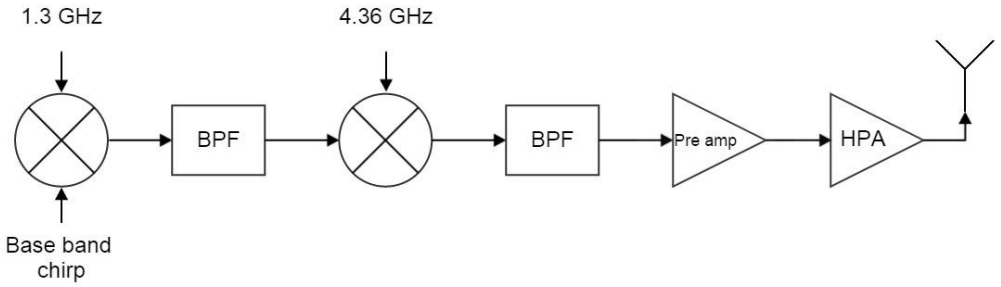

Figure 3.5: Block diagram of the up-converter.

The up-converter was built with the components listed in Table 3.3 and some attenuators (used before the HPA to regulate the power transmitted). Figure 3.6 shows the setup of the components on the radar.

The mixers were chosen because of their frequency range and price. For proper operation, the input chirp pulse at the mixers should be 10 dB lower than the LO power of the mixer. Thus, the chirp pulse at baseband is attenuated before the first stage of up-conversion. The L-band filter used has a very high roll-off in the high frequency stop-band which is important to attenuate the image frequency band at L-band. For the second-stage of up-conversion and RF filtering, since there were no

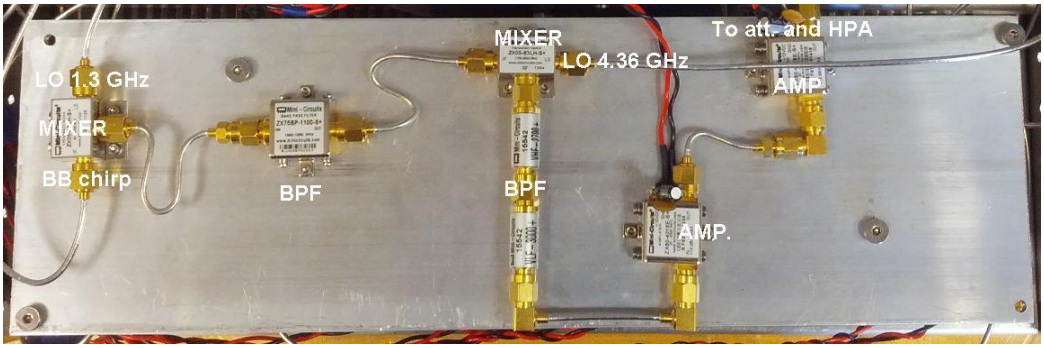

Figure 3.6: Up-converter. The BB chirp is up-converted (travels from the left to the right) and it is ready to be amplified in the HPA.

S-band bandpass filters that met the system needs, a low pass filter and a high pass filter are mounted in cascade. The S-band amplifiers and the attenuators are used to amplify the pulse to get the desired power at the antenna. If the power needs to be decreased, the radar enclosure has two external SMA connectors where more attenuators can be connected. Thus, this stage can be used to add attenuation before the pulse goes into the HPA. The HPA has a maximum output of 16 W. Higher power helps to be able to detect weaker targets, it also has the negative effect of worsening the saturation of the system due to the coupling between antennas.

3.1.9 Down-converter

When the signal is received, the down-converter will convert the received signal back to baseband. Immediately after the antenna, the received signal will pass through the Low Noise Amplifier (LNA) which is essential to have a good receiver Noise Figure (NF). The LNA is followed by a set of filters, mixers and an amplifier as shown in Figure 3.7 and Figure 3.8. These components are necessary to bring the signal back to baseband while increasing its power so that it can be digitally sampled.

Rejection of the image frequency is an important task of the down-converter. When choosing filters for image rejection, a trade off between a high rejection and a good phase linearity of the signal is necessary. For instance, if a filter with a very

Component type	**Specifications**	**Use**
Mixer	LO Power +10dBm, Conversion Loss 6.3dB	Up-conversion to L-band
Band Pass Filter	Fast roll-off on the upper side band, Passband= 1000-1200 MHz	LO and image frequency band attenuation
Mixer	LO Power +10dBm, Conversion Loss 5.6dB	Up-conversion to S-band
Low Pass Filter	Passband=DC-3600 MHz	Attenuate image frequency band
High Pass Filter	Passband=2500-6500 MHz	Clean lower side spectrum
Amplifier	Gain 16dB, P1=16dBm, IP3 =28dBm	Amplify the chirp pulse before the HPA
High Power amplifier	Gain 45 dB, P1=42.5dBm, IP3 =48.5dBm	Amplification before transmit antenna

Table 3.3: Components used in building the up-converter. All of them have SMA connectors.

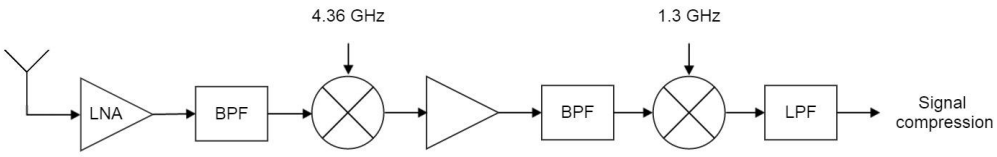

Figure 3.7: Block diagram of the down-converter.

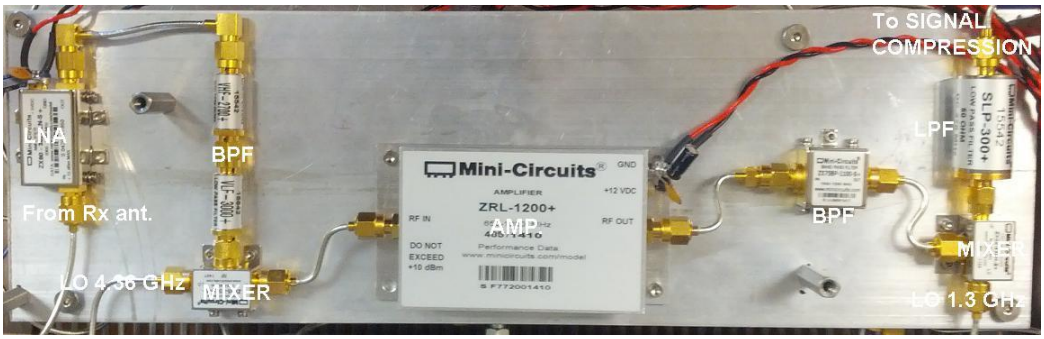

Figure 3.8: Down-converter. The received signal in the antenna enters the LNA. The pulse is down-converted (travels from the left to the right). Then, it is ready to get compressed.

sharp response is chosen, it will reject the image frequency band but its phase will be nonlinear. Non-linearities in the phase are a source of signal distortion through dispersion and will have a negative impact on processing of the data for interferometric applications.

Most of the components used in the down-converter and up-converter are similar. Table 3.4 lists the components used in the design. First, the LNA with a NF of 1.05 dB amplifies the pulse received without significantly increasing the noise floor. In order to minimize the impact of the radar system on the platform aerodynamics, the LNAs are connected with SMA cables to the receive antennas and mounted within the receiver enclosure. Consequently, the cables' 1.5 dB attenuation does have an effect on the NF of the system, but remains in an acceptable range. A low pass filter is included in the receiver to attenuate all of the intermodulation products that result from the down-conversion and amplification of the signal.

Component type	**Specifications**	**Use**
Low Noise Amplifier	Gain 20dB, Noise figure 1.05dB, P1=16dBm	Amplifier with low NF
Low Pass Filter	Passband=DC-3600 MHz	Reject image frequency band
High Pass Filter	Passband=2500-6500 MHz	Clean lower side spectrum
Mixer	LO Power +10dBm, Conversion Loss 5.6dB	Down-conversion to L-band
Amplifier	Gain 26dB, P1=24dBm	Amplify received pulse at L-band
Band Pass Filter	Fast roll-off on the upper side band, Passband=1000-1200 MHz	LO attenuation & image frequency band rejection
Mixer	LO Power +10dBm, Conversion Loss 6.3 dB	Down-conversion to base band
Low Pass Filter	Passband=DC-300MHz	Filtering before pulse compression mixer

Table 3.4: Components used in building the down-converter. All of them have SMA connectors.

3.1.10 Signal compression

Since the radar is used as an FMCW radar, a signal compression stage is needed. The signal compression creates the beat frequency waveform and amplifies the signal before it is sampled by the analog to digital converter (ADC). This stage is composed of a mixer, which outputs the beat frequency, a filter, responsible of reducing the noise bandwidth and rejecting unwanted signals resulting from the mix operation, and an amplification stage to make sure the signal is above the quantization noise level of the ADC. A block diagram is shown in Figure 3.9 and a photograph of the mounted components is shown in Figure 3.10.

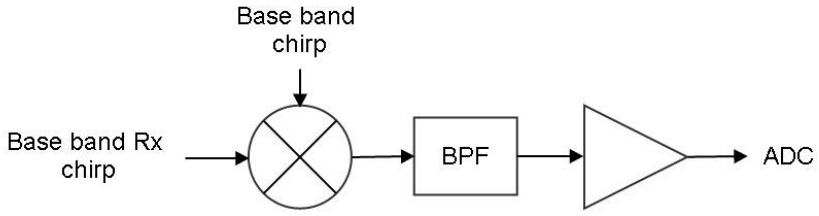

Figure 3.9: Block diagram of the signal compression stage.

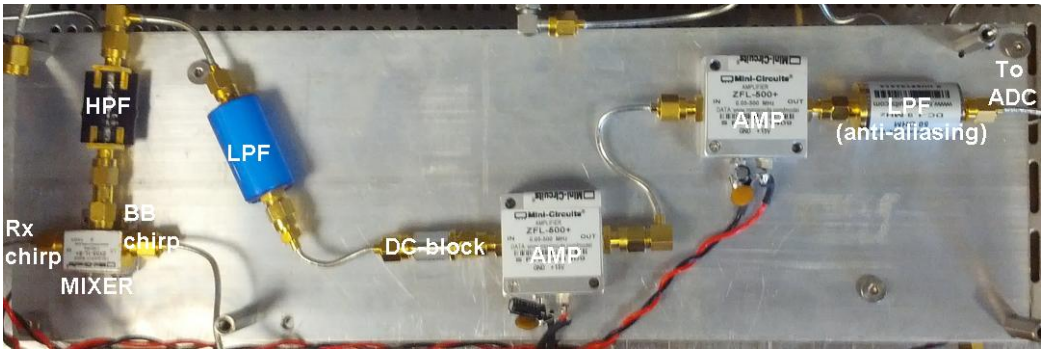

Figure 3.10: Signal compression. The received chirp comes from the down-converter and it is mixed with the BB chirp (before Tx) to get the beat frequency. After some filters and amplifiers, it is ready to be sampled.

The filter is a bandpass filter composed of a high-pass and a low-pass filter. The high-pass filter rejects the low frequencies containing unwanted high power signals

coming from the near-field coupling between antennas. Initially, a DC-block was used, but since the coupling was still very strong, a high-pass filter made in the laboratory was added. The low-pass filter (LPF) limits the bandwidth of the spectrum to sample, reducing the noise bandwidth integrated and minimizing the effect of aliasing.

The built signal compression stage contains the elements shown in Table 3.5. The high-pass filter was built on an FR4 printed circuit board (PCB) using surface mount device (SMD) capacitors and inductors. There are two low pass filters: one after the mixer and another one before the ADC. The first LPF has a cutoff frequency of 24 MHz. This filter rejects the higher frequencies coming out of the mixing operation to avoid having more intermodulation products after the amplifiers. Between the amplifiers and the ADC, another low-pass filter is used to reduce the potential of unwanted signals (e.g. intermodulation products of the amplifiers, bright targets at further range) to alias signals in the intended band. This filter is changed depending on the altitude that is flown. Flying at higher altitudes results in an improvement of the signal to noise ratio (SNR) of the targets at the far range. At lower altitudes, those targets have lower SNR due to the higher look angle. It is important to choose the right value of the filter to take into account the sampling frequency of the ADC. The frequency cutoff will be a few hundred kHz below half of the sampling frequency due to the roll-off of the filters.

3.2 Ground measurements

Before taking measurements from the airplane, the system was tested from the ground. Since at this stage, the radar was on its initial design, several measurements were done to characterize the system, to decide the appropriate chirp parameters, the position of the antennas and the acquisition configuration. The initial measurements were taken from the roof of the Lederle Graduate Research Center (LGRC) with a height of 60 m. The LGRC gives a privileged view of the UMass campus. However,

Component type	Specifications	Use
Mixer	LO Power +3dBm, Conversion Loss 5.7dB	Pulse compression, the output is the beat frequency
Low Pass Filter	Passband >200 kHz	Filter spurious signals
High Pass Filter	Passband >200 kHz	Reduce the near field coupled energy
DC block	Passband >100 kHz	Reduce the near field coupling
Amplifier	Gain 22dB, P1=10.9dBm	Amplify beat frequency before sampling
Low Pass Filter	Different passbands	Anti-aliasing filter

Table 3.5: Components used in building the signal compression stage. All of them have SMA connectors.

even at this height, the incidence angle from the roof is too close to grazing, and creates a lot of shadows and results in a poor SNR. Moreover, the low resolution in azimuth due to the antennas' beamwidth makes it particularly hard to discern individual targets in the radar's look direction. Nonetheless, the first results from early observations on top of the LGRT were useful to determine that the transceiver was working. The next step was testing the system at Mount Sugarloaf, a local mountain with sufficient facilities to support further testing of the system.

3.2.1 Setup

Mount Sugarloaf has a pavilion offering views of the Connecticut River, and the cities of Sunderland and Deerfield. The variety of targets (trees, fields, water, buildings, roads and mountains) makes Mount Sugarloaf a useful place to take measurements before setting up the system on the aircraft.

The measurements were taken pointing to two opposite sides: Sunderland and Deerfield. The Sunderland side gave better results since it offers the view of the river, which is an easy recognizable feature in the radar returns. Thus, the results presented will focus on this area, showed in Figure 3.11.

Figure 3.11: Google earth view of the area scanned in the ground measurements from Mount Sugarloaf.

The system was mounted in a rack mount: the radar, the power supply, the acquisition computer and the signal generator. Since the radar was not moving while taking the ground measurements, a positioner was used to scan the area with the antennas. The positioner is able to tilt vertically and to rotate horizontally. Therefore, the look angle can be adjusted and the chosen area observed.

In some of the measurements, the goal was to create a synthetic array of antennas to improve the resolution. In that case, the antennas were moved horizontally in a straight line by the technician where no positioner was used. Figure 3.12 shows the typical setup of the system.

During all of the measurements, the main problem that needed to be solved was the coupling between the transmit and the receive antennas. Thus, the setup of the antennas was changed several times to find the best spacing and positioning to avoid coupling between the receive and transmit antennas.

Figure 3.12: Deployment of the system at Mount Sugarloaf.

3.2.2 Results

This section presents the results of the ground deployments and discuss main issues of the system such as the coupling between the transmitter and the receiver.

The coupling between antennas saturates the receiver and, together with multipath, results in a ripple in the received signal as a function of distance from the antenna. Because of this effect, this signal is not decreasing its power at further range. Therefore, the SNR of the system (when deployed on the ground) is usually low and small targets are hard to see due to the poor sensitivity of the system. Figure 3.13 is a good example of how the power of the received signal does not decrease with range. In this measurement, an aluminum plate was installed above the transmitter to improve isolation between the transmit and receive antennas. In this

configuration, the channel closer to the transmitter is still influenced by the energy being transmitted, while the other channel is slightly improved.

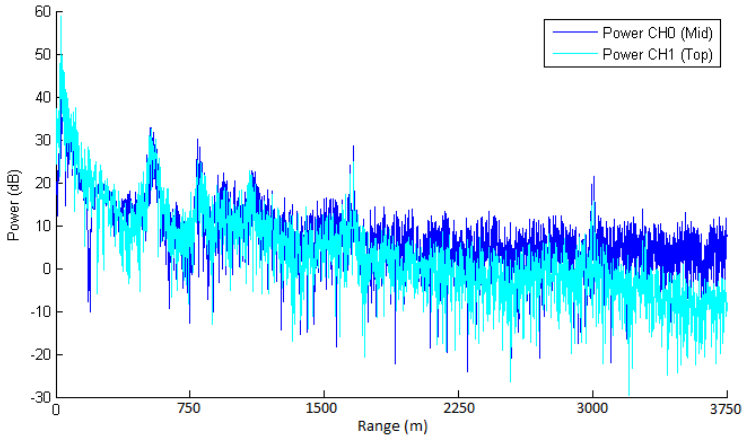

Figure 3.13: Spectrum of a ground measurement. The response of the same pulse is plotted for each channel. CH1 corresponds to the antenna which is situated farther from the transmitter. An aluminum plate was installed above the transmit antenna.

After correcting for the loss associated with range (i.e. dividing the observed power by a factor of $range^4$), this same effect can be seen in Figure 3.14. In this example, in the channel furthest from the transmitter some features can be seen, while in the channel closest to the transmitter (CH0), they are hard to notice. In this example, the reflectivity scale is calibrated using targets of known radar cross-section, however, this is not a critical parameter at this stage.

In order to reduce the effect of the near field coupling between the antennas, three different approaches to reduce this effect were used: reduce the transmitted power, separate the antennas, and isolate the antennas using a conductive plate between them. Reducing the transmitted power helps, but weak targets may not be detected since their response will be even weaker. Placing the transmitter antenna as far as possible from the receive antennas is also an effective solution. The transmitted power will remain the same while weaker targets will still be detectable. The disadvantage of this approach is that there is a limit to the distance between antennas due to spatial

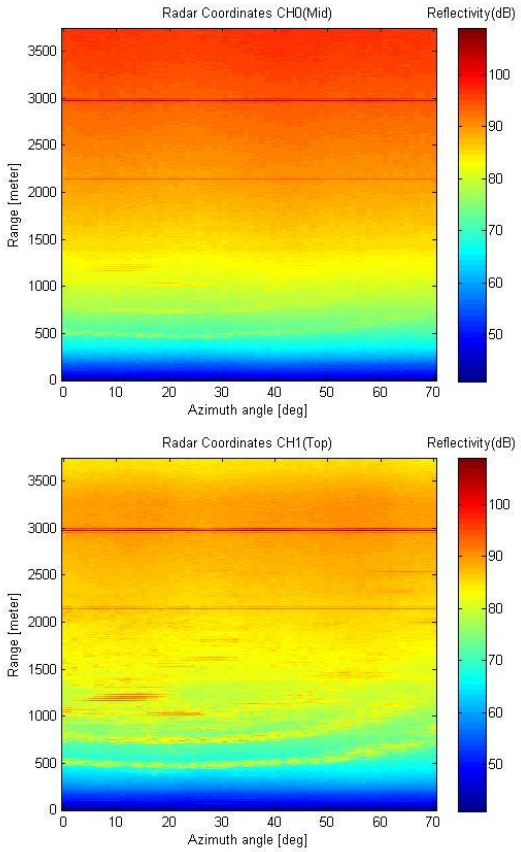

Figure 3.14: Ground measurement. Big near field coupling in CH0 which is closer to the transmit antenna.

limitations imposed by the physical size of the airplane door. Hence, the placement of a conductive plate between the transmitter antenna and the receiver antennas is a method of isolation that needed to be explored as well.

Figure 3.15 shows the measurement results after an aluminum plate was added above the transmitter. In this configuration, both channels have enough sensibility to detect different features. For example two lines of trees can be recognized along the river in the lower part of the image. The low transverse (azimuth) resolution of the system, estimated to be 12 degrees, makes it hard to distinguish between features in the images. This is because the transverse resolution in real aperture radar is determined by

$$\Delta R_{az} = R \cdot \theta_H, \tag{3.1}$$

where R is the range and θ_H the antenna's azimuth beamwidth. Recall, as discussed in Section 3.1.4, that θ_H is 0.21 radians. Hence, at a 1000 m range, the transverse resolution is $\Delta_{az} = 1000 \cdot 0.21 = 210$ m. This resolving power worsens at further range.

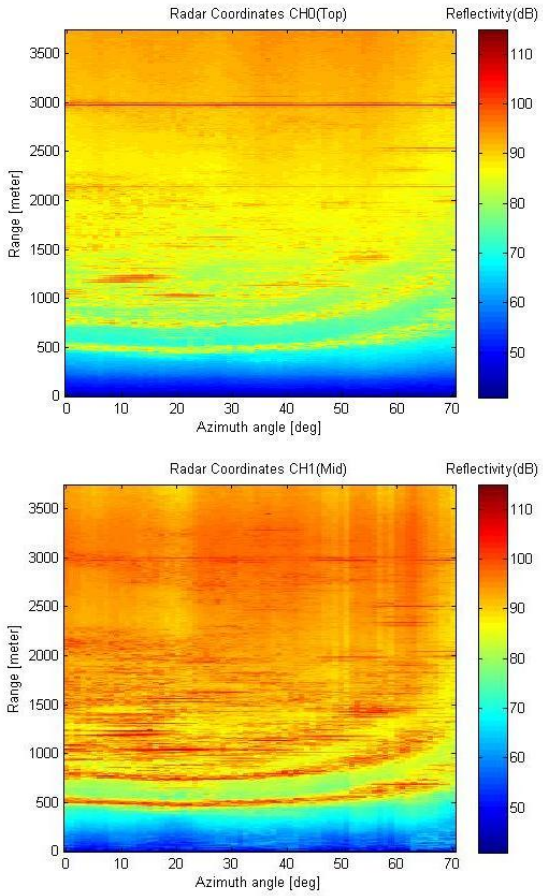

Figure 3.15: Ground measurement taken from Mount Sugarloaf. A plate was installed above the transmit antenna.

For this reason, in the development of the S-band system, it was desired to put the system on an aircraft in order to achieve a better viewing geometry (i.e. steeper incidence angles) and in order to form a synthetic aperture for improving the image resolution at far distances.

3.3 Flight measurements

Once the results from the ground measurements were shown to be repeatable, the next step was to bring the system to the airplane. This section presents how the system is installed in an aircraft and the results obtained from the first airborne measurements.

3.3.1 Setup

The most recent version of the integrated S-band radar and data system is shown in Figure 3.16 The compactness of this system reduces the time of installation and leaves sufficient room in the airplane cabin to install additional instruments if desired.

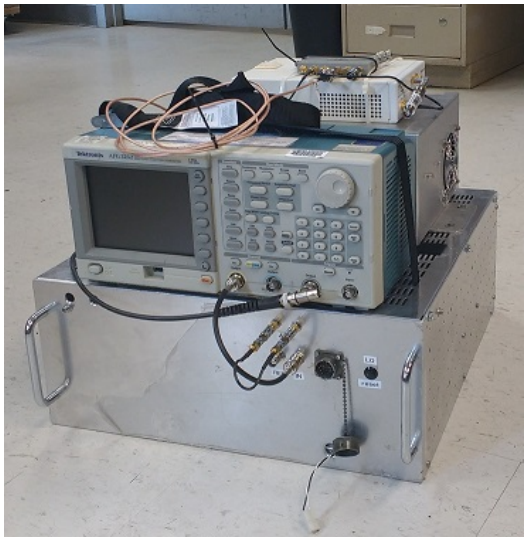

Figure 3.16: S-band transceiver, signal generator, Ettus board and power supply.

3.3.2 Flight lines and flight parameters

The flight path for the initial flights were so that features such as the river, trees, fields and buildings can be viewed by the radar. Thus the areas flown have been Western Massachusetts, with flight lines changed in different flights depending on the testing needs.

The altitudes flown have ranged between 500 meters to 2000 meters. Changes in altitude of this scale will change the response of the radar and hence several parameters need to be adjusted. For instance, a particular target seen from different altitudes will change the backscattered power because of the changes in incidence angle. Typically, when the incidence angle is small, the backscattered power will be higher than it would be with larger incidence angles, and hence small incidence angles will have a higher SNR than larger incidence angles. For this reason, when flying the same latitude/longitude patterns at higher altitudes, it is possible to increase the maximum range that the radar can see. Because of the smaller range of incidence angles, new targets in the far range might return sufficient power to be detected by the radar despite the fact that the range to the target is increasing. Because this is an FMCW radar, the sampling frequency determines the maximum range of the radar. Therefore, it is necessary to increase the sampling frequency when flying at higher altitudes and the anti-aliasing filter before the ADC. At higher altitudes the transmit power can be increased to compensate for the increased range loss. The nadir return which can saturate the receiver, and hence the maximum transmit power is usually chosen based on the power of this return.

The signal generator parameters used in all of the flight measurements are listed in Table 3.6.

3.3.3 Results

The flights have helped to improve the system, to learn what are the configurations that work better to avoid aliasing and non-linearities in the receiver, to maximize the swath, and to get better performance overall. Synthetic Aperture Radar (SAR) data processing for the system is currently developed and is not intended to be the main topic of this Masters thesis. At this time, not all of the data have been processed and there is still work that is ongoing. Figure 3.17 shows one of the images using real-

Function	
Sine	
Run Mode	
Sweep	
Amplitude Menu	
Amplitude	9 dBm
Offset	0 V
Sweep Menu	
Start Frequency	90 MHz
Stop Frequency	190 MHz
Sweep Time	1 ms
Return Time	0 ms
Hold Time	0 ms
Type	Linear
Mode	Trigger
Source	Internal
Slope	Positive
Trigger Interval	1.001 ms

Table 3.6: Tektronix AFG 3252 function generator flight configuration.

aperture processing and a close up with SAR processing. The range resolution is 1.5 m for both images since it depends only on the bandwidth of the pulse. The azimuth resolution for the real-aperture image depends on the beamwidth of the antenna and it is proportional to the range, as it is shown in Equation (3.1). The SAR processing achieves an ideal azimuth resolution of half the antenna length. For the processed image shown here, the azimuth resolution is 1.5 m.

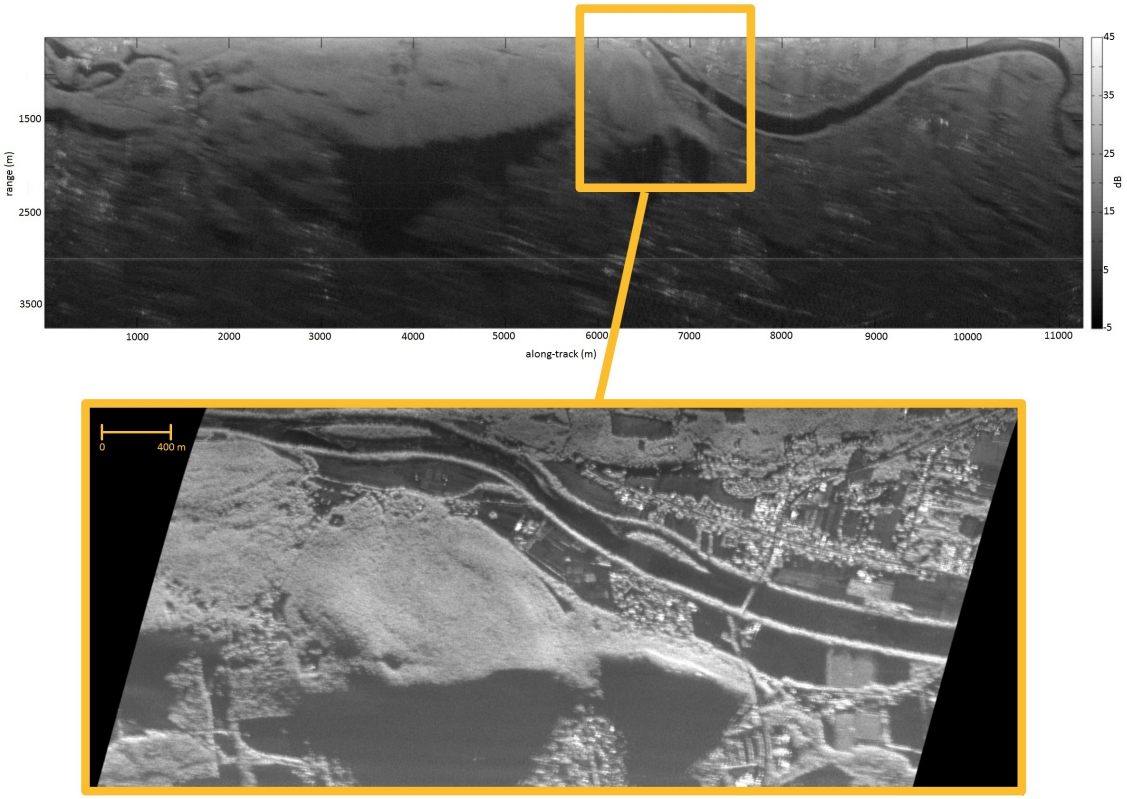

Figure 3.17: Real-aperture processing image and SAR processed close up.

CHAPTER 4

KA-BAND RADAR

The Ka-band radar described here is an FMCW 35 GHz radar with one transmit and two receive channels. It has been mounted on an airborne platform to be used as a side-looking interferometer as well as a nadir-looking scatterometer. A detailed description of the side-looking system can be found in [7]. This chapter describes the work done with the nadir-looking scatterometer during fall 2014 and spring 2015 and the systems transition to a side-looking interferometer that is combined with the S-band system presented in the previous chapter. It is anticipated that observations from the scatterometer will prove useful on their own and will be relevant to the side-looking interferometric configuration. The results might be useful in future processing of the Ka-band measurements as well as interpreting the results and errors associated with the interferometric measurements.

4.1 Data acquisition motivation and goals

NASA's Surface Water & Ocean Topography (SWOT) mission plans to measure the processes related to the global water cycle, the weather and the climate change. To get a better understanding of those processes, the SWOT mission will measure water storage changes in wetlands, reservoirs and lakes as well as global measurements of ocean surface topography [1].

The main instrument of the SWOT mission is a Ka-band Radar Interferometer (KaRIN). The interferometer will be near-nadir with look angles ranging from 0.6° to 3.9°. One of KaRIN's objectives will involve the measurement of the NRCS of different

water bodies as well as vegetation and other land surface cover. The instrument must be able to detect water-land transitions, hence the contrast between water and land surface needs to be studied and characterized. Lack of large studies at Ka-band with similar look angles motivates the work presented in this chapter. The Ka-band radar developed at MIRSL is used in a similar setup to acquire data that will help to study the response of the mentioned targets. Exploring the data over vegetation also showed potential for a different objective: tree height estimation. This topic is also explored in the following sections.

Therefore, the measurements focused on water characterize the NRCS as a function of look angle and wind speed. The data acquired over forest characterizes its NRCS response and is used to estimate tree height.

4.2 Nadir-looking scatterometer overview

The scatterometer uses the Ka-band radar transceiver and power supply from [7] with minor modifications. The transmit antenna is a rectangular horn and the receive antenna a dual-polarized Gaussian-optics lens (GOA-28-S00012D Millitech). The horn antenna has a large footprint while the receive antenna has a narrow beamwidth. The large footprint of the transmit antenna makes it easy to align the transmit and receive antennas. Because of the nadir configuration, the transmit power is kept at 1 mW to avoid saturation of the receiver due to the high RCS values of water for small look angles. The system parameters are shown in Table 4.1. Figure 4.1 shows the installation of the system on the airplane.

The acquisition system used for the scatterometer is the software defined radio, USRP N210, from Ettus Research , the same type that is used for the S-band radar. The signal generator used is the Tektronix AFG3252. The system also uses a Trimble Ag132 GPS and a DMS-EGP02 IMU to measure the position and platform motion.

(a) Scatterometer, signal generator, ADC and power supply.

(b) Transmit and receive antennas.

Figure 4.1: System mounted on the Cessna 206.

Moreover, an optical camera was installed to provide a record of the ground conditions during the time of observation.

To get accurate measurements of the radar cross section, the system is calibrated on the ground before each flight. The calibration characterizes the receiver gain, antennas gain and other system parameters. The calibration needs a target with a known RCS, the distance from the radar to the target, the transmit power and the received power. The antennas are pointed to a trihedral corner reflector and

Parameter	Value
Transmitting antenna beamwidth	16^o(min)
Receiving antenna beamwidth	2.1^o
Center frequency	34.945 GHz
Wavelength	8.6 mm
Bandwidth	100 MHz
Noise figure	9 dB
Transmit power	1 mW
Range resolution	1.5 m
Pulse repetition frequency	1 kHz

Table 4.1: Ka-band scatterometer system parameters.

the transmit power is measured using a power detector (and verified using a power meter).

After calibration, the scatterometer was flown on a Cessna 206 platform, with the antennas pointing downward from the aircraft belly port. Targets such as water (Quabbin Reservoir and Connecticut river) and forests in Western Massachusetts with and without snow were observed. The altitudes for these flights were kept between 150 m and 600 m in order to have a small antenna footprint to focus on targets with homogeneous scattering characteristics.

4.3 Geometry

The measurements of the system needed to resemble the satellite's setup to be meaningful. The data collection must cover the look angles of the satellite configuration. The system was mounted on the airplane and both antennas, transmit and receive, were mounted on the belly port of the airplane as shown in Figure 4.3c. Thus, the antennas were nadir-looking (i.e., antenna beam perpendicular to Earth's surface). This setup enabled coverage of the range of KaRIN look angles. Figure 4.2 shows the geometry of the setup.

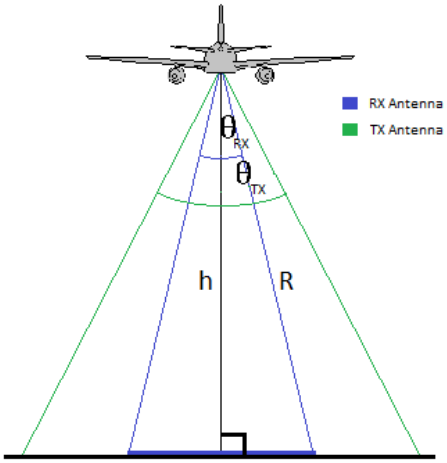

Figure 4.2: Nadir-looking geometry. Θ_{RX} and Θ_{TX} are the beamwidth of the receive and transmit antennas. h is the altitude of the radar and R is the range to the edge of the receive antenna's footprint.

If ideal conditions were given in a flight track, assuming both antennas are aligned and perfectly looking toward nadir, all of the data would fall at 0°. In a real flight, turbulence occurs naturally. The Cessna 206 is a light airplane where motion on its three axis is common even on calm days. While this could affect the quality of the data on other setups and measurements (i.e., SAR side-looking configuration), in this experiment it is taken as an advantage. The variance of the motion helps to cover the range of look angles of interest, as can be seen in Figure 4.3. Thus, the pilot normally does not need to focus on flying at a certain angle in any of the axes.

A perfect setup for any system is difficult to achieve and this one is no exception. When more samples of certain angles are needed, the acquisition is limited by atmospheric conditions as well as the pilot's ability to reduce the variance of the motion. Moreover, as can be seen in Figure 4.3, the distribution of angles is not uniform and consequently, some angles of interest might not be well sampled.

Installing the antennas perfectly pointing to nadir is difficult with the available tools. While this is not necessarily a flaw (no matter where the antennas point as long as the whole range of look angles is covered), the exact pointing (i.e., offset from real

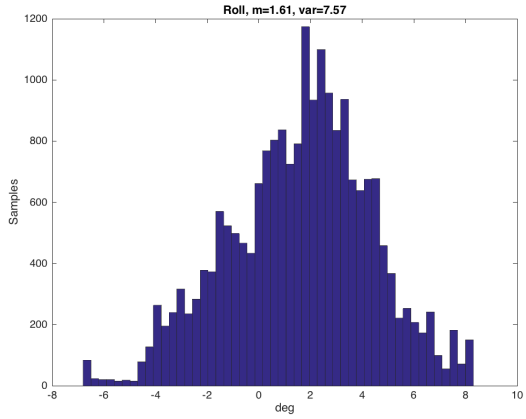

(a) Roll histogram for a flight line.

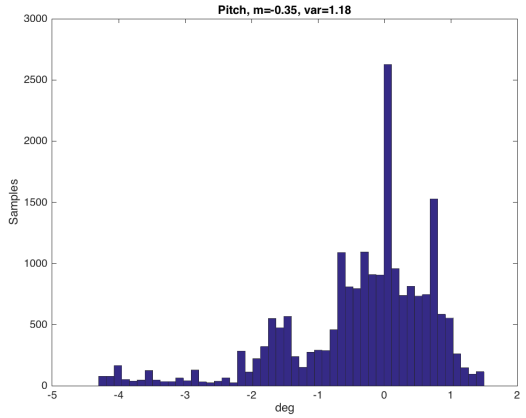

(b) Pitch histogram for a flight line.

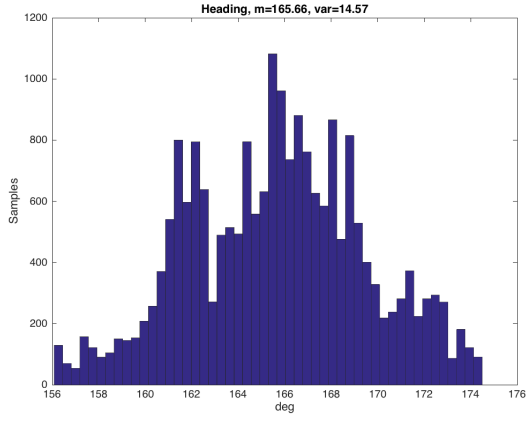

(c) Heading histogram for a flight line.

Figure 4.3: Aircraft motion histograms taken from a straight flight line.

nadir) is needed to correctly classify the pulses. While it can be hard to measure the offset in-situ, it can be inferred from the data. That is, the NRCS response for calm water is expected to be higher when the incident wave propagation is perpendicular to the water's surface, hence, the data can be corrected for the offset by looking for the maximum value of the NRCS response.

As mentioned in Section 4.2, the receive and transmit antennas have different beamwidths. The transmit antenna has a large beamwidth compared to the receive antenna. Therefore, even if the alignment between the antennas is not perfect, the receive antenna footprint falls within the large transmit antenna footprint. Thus, the resolution-cell of the system depends on the receive antenna pattern. For this reason, from now on, the receive antenna footprint will be referred to as simply the "footprint".

While for a side-looking radar the resolution-cell depends on the azimuth antenna beamwidth (if SAR processing is not applied) and the range resolution, this is not the case for the nadir-looking scatterometer. The footprint projected to the illuminated surface can be approximated by an ellipse, which will determine the resolution in both along-track and cross-track directions. The range resolution of the radar plays a different role. Since the look angles are small and the platform altitude is low, the backscattered power from the illuminated surface falls within one range bin. As it can be seen in Figure 4.4a, the altitude of the radar, h and the range to the edge of the footprint, R are not the same. However, since a range bin has a range resolution of $\Delta r = 1.5$ m, both distances fall within the same range bin. The main exception to this situation is given when volume scattering is present as can be seen in Figure 4.4b. Volume scattering will cause the received power to spread to different range bins. This property will be explored in future sections.

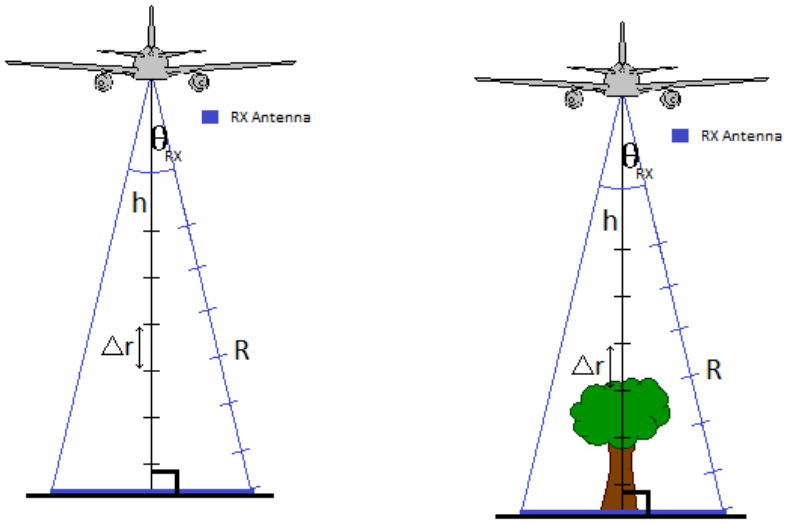

(a) Range without volume scattering.

(b) Range with volume scattering

Figure 4.4: Nadir-looking range resolution.

4.4 Calibration

The system needs to be calibrated for accurate and repeatable measurements. The calibration characterizes the receive and transmit antenna gain, the receiver gain and other system parameters. The result of the calibration is a value represented by the radar constant, which is inferred from the radar range equation

$$P_r = \frac{P_t G_t G_r \lambda^2 \sigma G_{rcv}}{(4\pi)^3 R^4}, \tag{4.1}$$

where P_r is the power received after the pulse compression, P_t is the power transmitted, G_t is the transmit antenna gain, G_r is the receive antenna gain, λ is the wavelength, σ is the radar cross-section, G_{rcv} is the gain of the receiver and R is the range of the target.

The radar range equation can be rearranged to get the radar constant equation. On one side there are the antenna's gains, the receiver gain, the wavelength and a constant

$$K_r = \frac{\lambda^2 G_t G_r G_{rcv}}{(4\pi)^3}. \tag{4.2}$$

Notice these are the elements that need to be characterized and that are affected by, for instance, the temperature. The other side of the equation is defined as

$$K_r = \frac{P_r R^4}{\sigma P_t}, \tag{4.3}$$

and it is used to measure the combined contribution of the system elements. The radar constant is then calculated using a target with known RCS, placed at known range, and measuring the transmitted and received powers.

For the Ka-band scatterometer, the entire calibration is done on the ground, before and after each flight. Once the system temperature is stable, a corner reflector with a well defined RCS is placed at a measured distance from the radar. The transmitted power is monitored with a power detector and verified with a power meter. Finally, the power spectral density is computed using the periodogram estimator with a flat-top window, the power corresponding to the corner reflector is integrated and the received power estimated. The radar constant is calculated and used in the flight data processing.

Two corner reflectors, shown in Figure 4.5, with different cross-sections were used.

The radar constant obtained for different calibrations done the same day are shown in Figure 4.6. Two calibrations were done using the small corner reflector ($RCS = 1.94m^2$) and one using the big corner reflector ($RCS = 596m^2$). The distance from the radar to the corner reflectors was different for each measurement. Calibrating using different corner reflectors and at different range gives a more accurate result, since the effect of multipath, movement or misalignment can be reduced. The discrepancy in the mean between measurements can be explained by the misalignment between the receive antenna's maximum and the corner reflector and by multipath reflections. The difference in standard deviation can be explained by wind (moving the corner reflector

(a) Corner reflector, $RCS = 1.94m^2$.

(b) Corner reflector, $RCS = 596m^2$.

Figure 4.5: Corner reflectors.

and/or the antenna) and by people crossing between the antenna and the corner reflector. The three measurements are considered as valid and the mean between them is used as the calibration radar constant.

4.5 Flight plan

The flights planned for the scatterometer had different goals and can be divided into two categories: engineering and science flights.

The first flights were engineering flights. These were planned to be short and the goal was to test the system: radar and supporting electronics such as GPS, IMU and data acquisition. While the primary goal of these flights was not science data collection, the flight lines were chosen to resemble a science flight. The flight lines flown considered different aspects of the geometry (i.e., size of the footprint) as well as the targets observed. The lines were flown over the Connecticut River and the Quabbin Reservoir. Most of the flight time was spent over the Quabbin Reservoir where water and vegetation can be easily measured. Figure 4.7 shows the flight track over the Quabbin Reservoir. The altitudes chosen were 300 m and 600 m. At these altitudes, the footprint is small enough to measure targets with homogeneous scattering properties. Note that the flight track has several island crossings intended to be used to measure water-vegetation contrast.

The data acquired on the second engineering flight was valid for statistical measurements and the following flight plans, considered science flights, focused on new targets. Data on more water-land crossings was needed as well as new water bodies. Thus, the new targets were mainly streams and ponds.

All of the flights were conducted between November 2014 and July 2015 which gave a wide range of ground conditions, for instance snow, ice, leafless or blooming trees, among others.

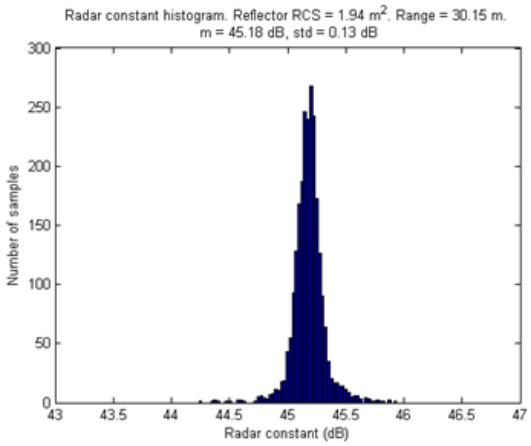

(a) Corner reflector, $RCS = 1.94\,m^2$, $range = 30.15\,m$.

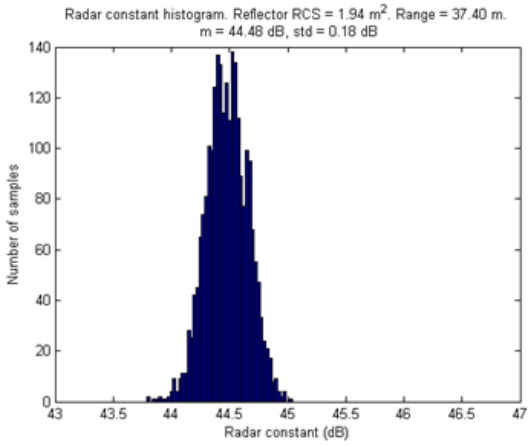

(b) Corner reflector, $RCS = 1.94\,m^2$, $range = 37.40\,m$.

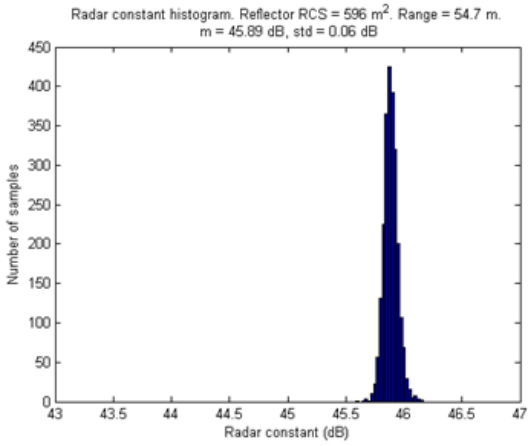

(c) Corner reflector, $RCS = 596\,m^2$, $range = 54.7\,m$.

Figure 4.6: Calibration histograms for three different setups.

Figure 4.7: Flight track over Quabbin Reservoir.

4.6 Data processing overview

The data are collected in 2 minute length files, roughly 1 GB each, with flights typically generating 50 GB of data. This large amount of data requires some processing before it can be used to get final products such as Normalized Radar Cross Section (NRCS) estimation and classification. The data processing consists of several Matlab functions. The first functions read the raw scatterometer data, the GPS data and the IMU data. The GPS and IMU datasets are resampled to the pulse rate. The datasets are merged to geolocate each of the received pulses. The calibration is applied, the swath location and area are calculated and the NRCS is estimated. Moreover, using the MassGIS-Land Use data, the target of each of the pulses can be classified (water, forest, crop, buildings...). This data is saved in a '.mat' file for each of the lines. Generating these files, for the second flight, takes 3 hours without target classification and 7 hours with. Figure 4.8 shows the block diagram for the processing algorithm. Once the files are generated, it is easy and quick to generate statistics using the NRCS, the classification and the IMU data.

4.7 Raw data processing

The raw scatterometer data is a sampled time-domain waveform that results from the FMCW pulse compression. The time-domain waveform needs to be transformed to the frequency domain to map it into range and to get the returns associated with each pulse. Thus, to correctly estimate the power received, it is necessary to estimate the power spectral density. While there are several estimators that can be used for this purpose, the periodogram is a simple estimator and is easy to implement. The results presented here use the periodogram estimator. Its main downside is a high variance compared to other estimators such as Bartlett's method. An error budget in the NRCS estimation will determine if the variance of the power spectral estimator

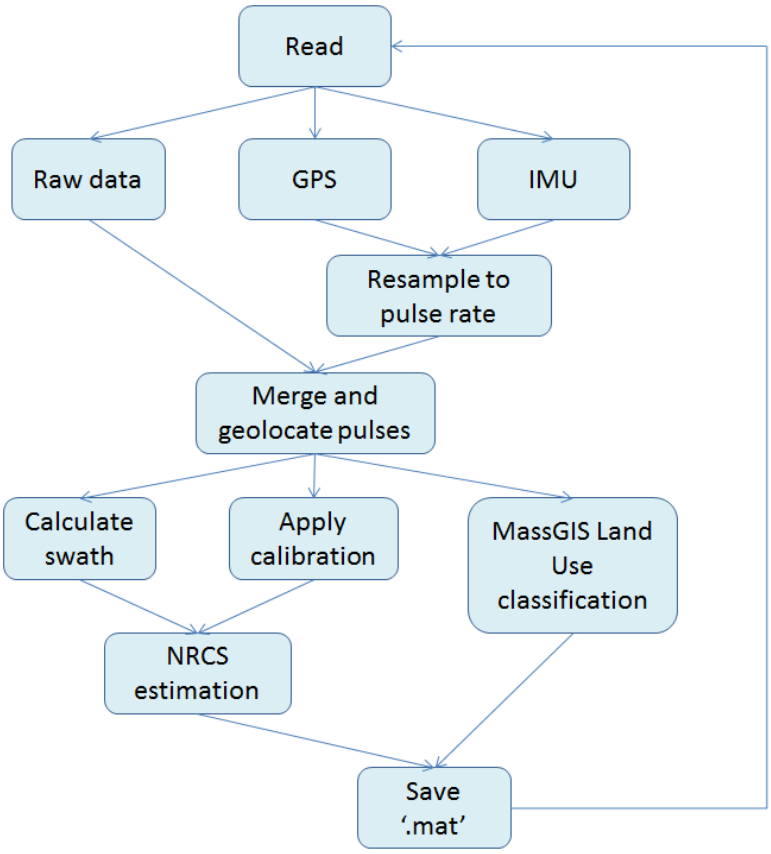

Figure 4.8: Ka-band scatterometer data processing block diagram.

has a large impact in the overall measurement and if another power spectral estimator should be used.

4.8 Normalized Radar Cross-Section estimation

The Radar Cross Section σ, is calculated using the radar equation:

$$P_r = \frac{P_t G_t G_r \lambda^2 \sigma}{(4\pi)^3 R^4}. \tag{4.4}$$

In the results presented in this work, the antenna gain is assumed to be uniform over the projected area. Thus, the Normalized Radar Cross Section, σ^o, can be calculated as:

$$\sigma^o = \frac{\sigma}{A}, \tag{4.5}$$

where A is the illuminated area by the antenna beamwidth.

The calibration determines the radar constant K_r:

$$K_r = \frac{\lambda^2 G_t G_r}{(4\pi)^3}. \tag{4.6}$$

The NRCS is then calculated as:

$$\sigma^o = \frac{P_r R^4}{P_t K_r A}. \tag{4.7}$$

- $\mathbf{P_r}$. The power received. Calculated using the periodogram and integrating over the peak's neighboring range bins. The power of the target is spread because of the window's resolution. Hence, the power in the range bins surrounding the peak is summed into the peak's power to get the total power of the target. In the case of water, the power of the main peak is integrated. For volume scattering targets such as trees, the power integrated corresponds to the maximum peak return.

- **R**. The one-way distance the pulse has traveled. In FMCW radar, it is calculated in the frequency-range domain. Note the mapping between frequency and range described by Equation (2.10) is used here. The range resolution is

$$\Delta r = \frac{c}{2B} = 1.5 \text{ m}, \tag{4.8}$$

where c is the speed of light and B the bandwidth of the chirp. The product of the peak's frequency bin and the sweep time, $f_{peak} \cdot \tau$, is found and the distance is then calculated as

$$R = \tau f_{peak} \Delta r. \tag{4.9}$$

- $\mathbf{P_t}$. The power transmitted. The results presented in this work assume the transmitted power is constant and therefore, it is included in the radar constant. In future versions of this scatterometer, an installed power detector is used to measure the transmitted power on a pulse-by-pulse basis.

- $\mathbf{K_r}$. The radar constant. This constant is determined through the previously described calibration approach where a corner reflector with a known RCS is measured. The knowledge of the distance, power transmitted and power received allows to measure the radar constant:

$$K_r = \frac{P_r R^4}{P_t \sigma}. \tag{4.10}$$

- **A**. The area of the projected antenna beamwidth. Using the IMU, GPS and radar data, the pulses are geolocated and hence, the swath's area estimated. To decrease the computational time, the swath is sampled with a few points. Once it is projected to the ground, the distance $d_r = d\big(xyz, x_0 y_0 z_0\big)$ from each of the

points to the center is computed. The swath is approximated as an ellipse and hence, the area can be calculated as

$$A = \pi \cdot d_{r_{max}} \cdot d_{r_{min}}. \tag{4.11}$$

4.9 Normalized Radar Cross-Section analysis

The SWOT mission will measure the NRCS of different water bodies and will detect water-land transitions based on NRCS measurements. The data collected for this work contributes to study the response at Ka-band of inland water at different look angles and wind speeds.

There are existing models that can be used to predict the response of the NRCS over water as a function of look angle and wind speed [9]. Using the land use classification from MassGIS, the pulses over the water are identified. The transitions between land and water are filtered out. The measured NRCS over water as a function of look angle is plotted in Figure 4.9. Note that the data used corresponds to the whole dataset acquired in one flight. The data fit the model described at [9] for inland water bodies when the average wind speed is 2 m/s. Notice that to fit the data to the mentioned model, mss_h is used instead of mss_{Ka}. The latter, mss_{Ka}, has the contribution from long-wavelength waves and short-wavelength. However, the contribution from long-wavelength waves is small for inland water bodies. The average wind speed was corroborated using ground truth wind data over the area.

In order to characterize the water-forest transitions, the NRCS measurements over land are processed. The NRCS over forest and ground does not show a clear dependency on the incidence angle (Figure 4.9b). Notice that the power integrated corresponds to the main peak of the return, which usually corresponds to the ground return. The losses due to the trees are not taken into account.

It is worth comparing Figures 4.9a and 4.9b. The NRCS difference, or NRCS contrast, between water and forest can be approximated to 23 dB at look angles ranging from 0° to 3.5°. However, due to the angle depency of NRCS over water, this contrast is reduced with increasing angles. Since SWOT's look angles are not higher than 4°, the angle dependency should not limit the instrument's capability for detecting the transitions. For the data presented here, it is possible to detect water-forest transitions just by setting a threshold on the NRCS value. Nevertheless, this example only covers a very specific case. For instance, the contrast will likely be different if there are higher wind speeds (water response has shown to be different [9]). Other elements such as moisture or ice will also change the NRCS causing the contrast to change. This is why further study of the acquired data is needed. Furthermore, new data collection should focus, for instance, on different wind speeds and land cover types.

4.10 Spectrum waveform analysis

The study of the waveform in the range domain has showed that the nature of targets can be inferred from the shape of the backscattered pulses. At Ka-band, results have shown that pulses get backscattered by targets such as trees' branches and leaves. The applications derived from this are many. For instance, it can be used to classify targets or to estimate terrain height and the height of trees. Furthermore, it can be useful to estimate errors in phase that are induced by the volume scattering properties of targets that need to be taken into account for interferometry. An example of a typical vertical reflectivity profile over water and vegetated land surface (for the Quabbin Reservoir) is shown in Figure 4.10. It is easy to see the crossing of islands, the scatter of trees and water as well as other artifacts.

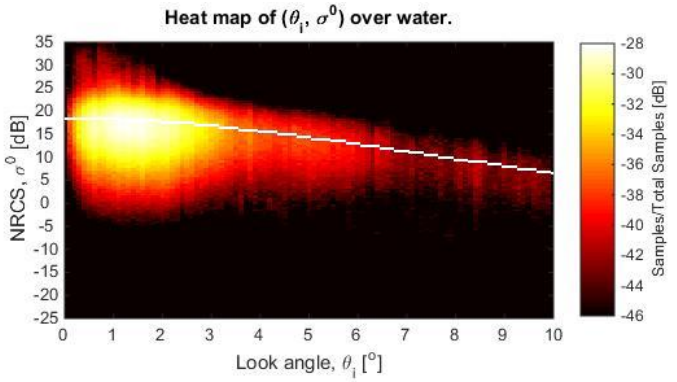

(a) NRCS over water.

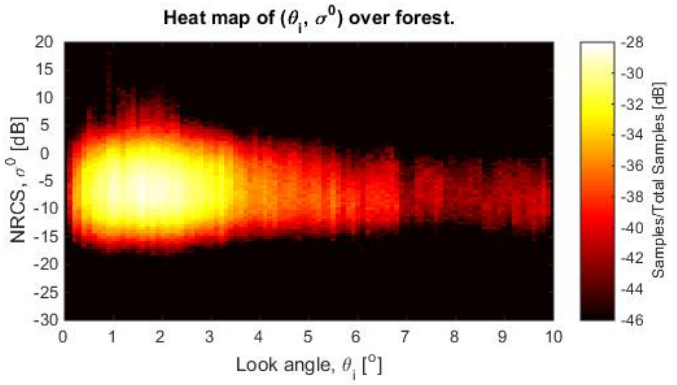

(b) NRCS over forest area.

Figure 4.9: Normalized radar cross section as a function of look angle. In plot (a), the white line represents the model presented in [9].

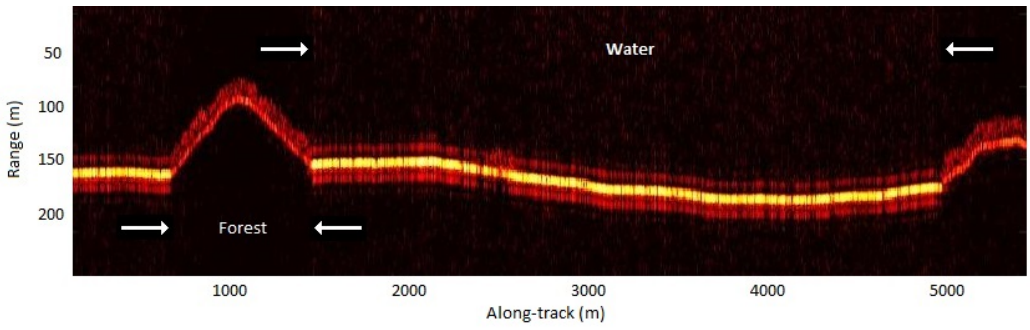

Figure 4.10: Non-scaled spectrum over the Quabbin Reservoir. The highest power is backscattered from the water.

4.10.1 Trees frequency waveform and tree height estimation

At 35 GHz, it looks like the radar is sensitive to different elements of the trees. Thus, the response is a series of peaks as shown in Figure 4.11. Figure 4.13 gives a closer look at the radar return as a function of range when flying over one of the Quabbin Reservoir islands. Notice that the peaks are distributed over several range bins. For the side-looking radar setup, each pixel in a forested area (volume scattering target) will have contributions from the targets inside the area as well as contributions due to the scattering of trees in the surrounding pixels. If these observations were interpreted as coming from a surface, this will lead to errors both in phase and RCS estimation. Further analysis of the data collected with the scatterometer might help to minimize the effect of these errors in the measurements.

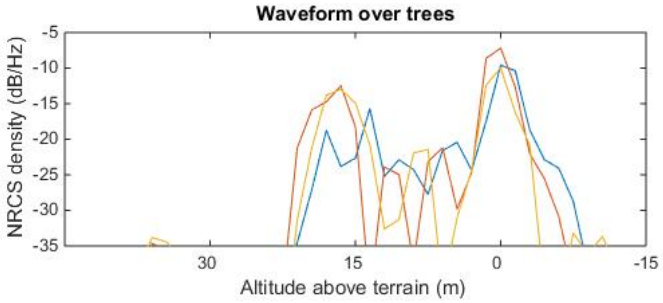

Figure 4.11: Waveform over trees for three different pulses.

Such data can be used for the estimation of tree heights as well. This process is based on the following assumptions:

- The strongest peak usually corresponds to the ground return. In some cases, the strongest peak is one of the first returns and it is believed to be related to the foliage of the trees.

- The rest are due to backscatter from branches, trunks or foliage.

The algorithm locates the maximum return in the spectrum and detects the peaks above the noise level, which results in the backscattered waveform. After additional filtering, the algorithm follows the block diagram shown in Figure 4.12.

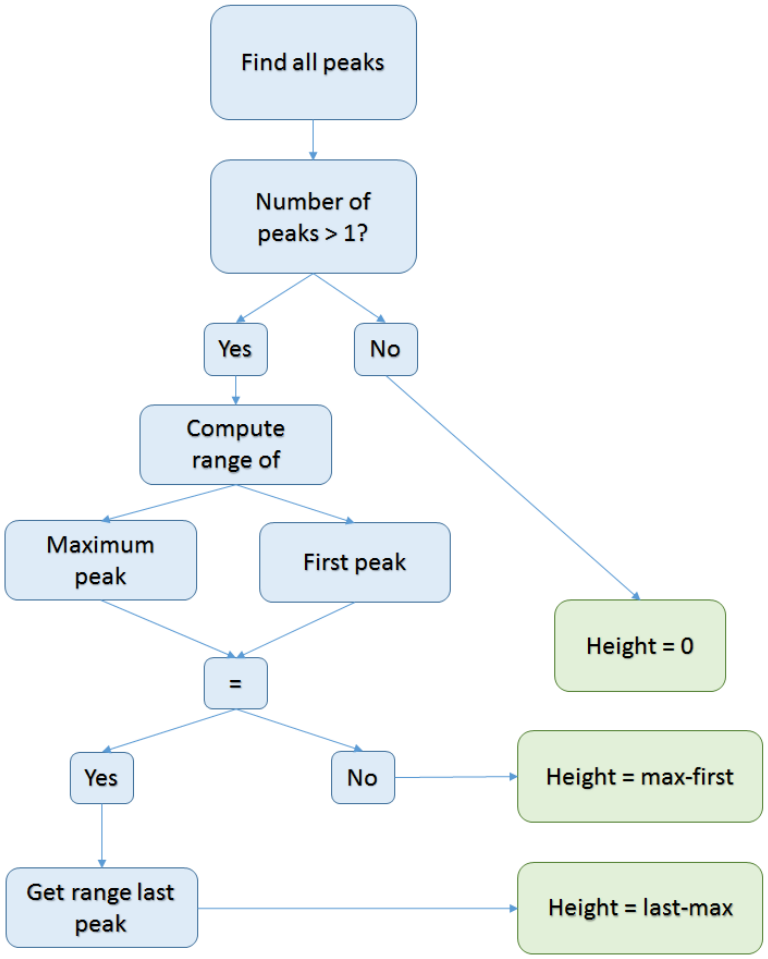

Figure 4.12: Tree height algorithm block diagram.

The histogram of the estimated tree height for an island on Quabbin Reservoir is shown in Figure 4.14. The values for tree heights are reasonable for the area, although no existing datasets with similar resolution exist.

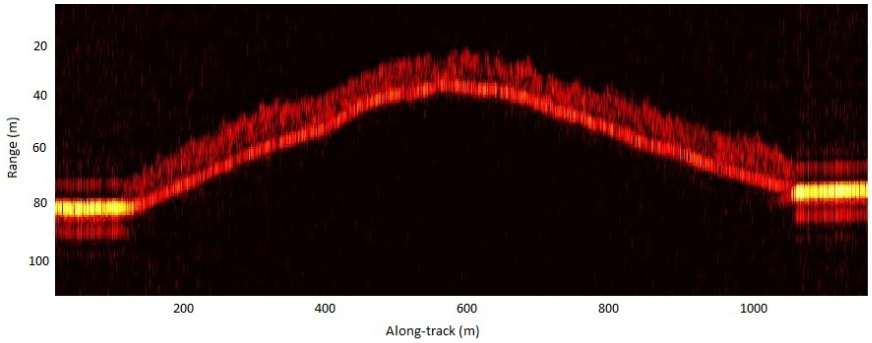

Figure 4.13: Non-scaled spectrum over forest.

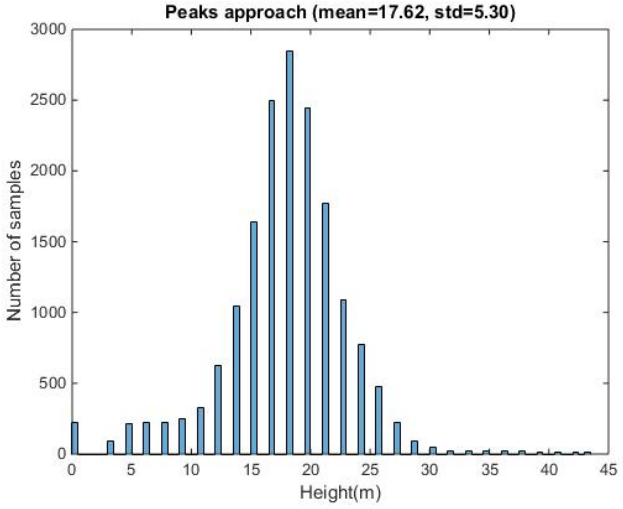

Figure 4.14: Estimated tree height histograms.

CHAPTER 5

KASI: KA-BAND AND S-BAND CROSS-TRACK INTERFEROMETER

A dual-frequency system using both the S-band and Ka-band radars is of interest for a variety of reasons. Two systems working at different wavelengths acquiring data simultaneously will give a valuable dataset since the conditions on the ground will be exactly the same. Hence, elements such as wind, soil moisture or any other changes on the ground will not interfere in the measurements. Differences in RCS can be studied to determine if elements such as soil moisture or foliage density can be inferred or estimated more precisely from the combination of the datasets at two different frequencies. Interferometric measurements using the dual-frequency system could be used to get a better estimation of tree height or snow depth.

5.1 System overview

The dual-frequency system described here combines the existing S-band and Ka-band transceivers and the supporting electronics to build a system that can be mounted on an airborne platform to acquire data at the two frequencies simultaneously. Each of the transceivers is kept separate and the efforts to reduce system weight and volume focus on combining the supporting electronics. Figure 5.1 shows the block diagram for the dual-frequency system. The system needs to be synchronized to the same timestamps and need a common reference signal. Thus, the two GPS units, the IMU, the 10 MHz reference signal and the signal generator are common for both radars. Each of the transceivers uses an Ettus Research USRP N210 as

Parameter	Ka-band	S-band
Azimuth antenna beamwidth	1°	12°
Center frequency	34.945 GHz	3.2 GHz
Wavelength	8.6 mm	93.75 mm
Bandwidth	100 MHz	
Max. transmit power	1 mW	16 W
Range resolution	1.5 m	

Table 5.1: Dual-frequency system parameters.

an ADC which allows for two sampling channels. Furthermore, each radar uses a different laptop where the sampled data is saved into a solid state hard drive. Moreover, each radar has three antennas: one transmit and two receive.

One of the GPS units is just used to set the timestamps to the data by using the PPS (Pulse Per Second). The other is used to geolocate the pulses (i.e., latitude, longitude, altitude data). The 10 MHz reference signal is used in the signal generator, the Ettus ADC board, and the transceivers. For the system to be coherent, it is necessary to have a common reference that drives the pulse generation, the local oscillators and the data acquisition. The signal generator has two output channels that allow for two separate chirp generation. The chirps are synchronized and of equal sweep time. Every time a new pair of chirp pulses are generated, a TTL rising trigger is sent to the acquisition system. The sampled data is saved into the hard drives of two laptops, one laptop for each radar. The Trimble GPS data is logged into one laptop while the IMU data is logged into the other one. By using two laptops, the system can have higher sampling rates, which are necessary when flying at high altitudes, and all the elements of the system (i.e., two radars, GPS and IMU) can be closely monitored.

The parameters for each radar are listed in Table 5.1.

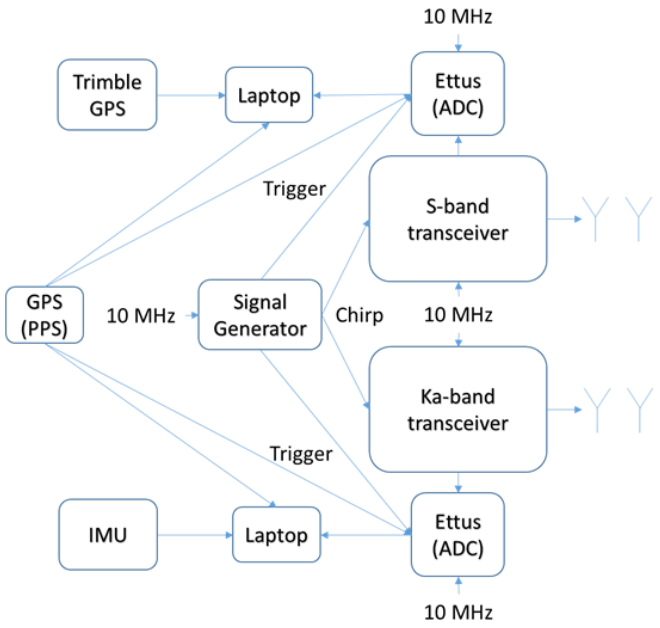

Figure 5.1: Block diagram dual-frequency system.

5.2 Antennas

The antennas used in the dual-frequency system are the respective antennas for the side-looking configuration of each system. Each of the two transceivers have two receive channels and hence, three antennas are needed: one transmitter and two receivers. A detailed description of the S-band antennas can be found in Section 3.1.4. The Ka-band antennas are slotted waveguide antennas with an azimuth beamwidth of 1° and 45° in elevation.

The antennas of both radars were mounted on the airplane. To be able to illuminate the same area, they need to point to the same side as well as have similar look angles. The mounted antennas can be seen in Figure 5.2. The plate used to mount the S-band antennas was used as the base structure. The two receive S-band antennas were mounted on this plate. The structure used in the past to mount the Ka-band antennas was mounted on the S-band plate to accommodate the two Ka-band receive antennas. The Ka-band transmit antenna is mounted on the bottom of the same plate. The S-band transmit antenna is mounted on the belly port of the airplane.

Figure 5.2: Antennas installation on the airplane. The top antenna is the first S-band receiver. The next two are the two Ka-band receive antennas. Next, the second S-band receive antenna. The Ka-band transmit antenna is mounted at the bottom. The S-band transmit antenna is mounted on the belly port of the airplane.

The disposition of the antennas was decided taking into account the coupling between antennas and the phase sensitivity. The S-band transmit-receive coupling and multipath due to the airplane structure have been always a problem. Therefore, the S-band transmit antenna was placed as far from the receivers as possible. The separation between the receive antennas (baseline) was chosen based on the phase sensitivity and height ambiguity. The baseline for the S-band antennas is 0.76 m giving a height ambiguity of 187 m and phase sensitivity of 0.034 rad. The baseline for Ka-band is 0.18 m giving a height ambiguity of 71.4 m and phase sensitivity of 0.088 rad.

5.3 Side-looking geometry: stripmap mode

The system can be deployed and mounted on an aircraft using different viewing geometries. The dual-frequency system is always mounted in a side-looking geometry. Different modes can be found in the side-looking geometry: stripmap, spotlight, circular, scanning and squinted. The setup and processing used in this thesis is the stripmap mode, shown in Figure 5.3.

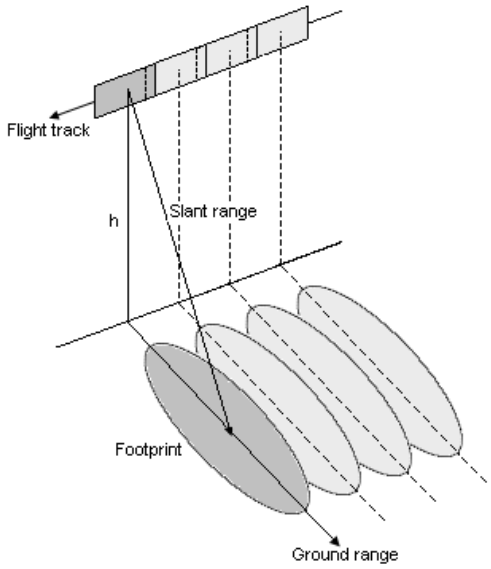

Figure 5.3: Side-looking geometry: stripmap mode.

A typical side-looking geometry consists of an airborne platform flying at a constant velocity in a certain trajectory with the antennas pointed to the side. In stripmap mode, the antennas are pointing perpendicular to the trajectory, which is linear. The antenna beamwidth is projected to the Earth surface on what is known as the illuminated footprint. The surface that is being imaged is called the ground plane. Alternatively, it can be understood as the projection of the slant-plane to the ground, where the slant-plane is the plane defined by the consecutive range lines, each corresponding to a single radar pulse, along the flight trajectory.

Due to this viewing geometry, two features are common in the data: layover and shadowing. When a radar pulse reaches the highest point of target (i.e., mountain

peak) before the lowest, the top point will appear at a closer range than the base. This will result in an image distortion known as layover, seen in Figure 5.4a. Shadowing occurs when the antenna beam is partially blocked by a high target as it is shown in Figure 5.4b. The following range bins are noise since there is no energy backscattered on that certain area.

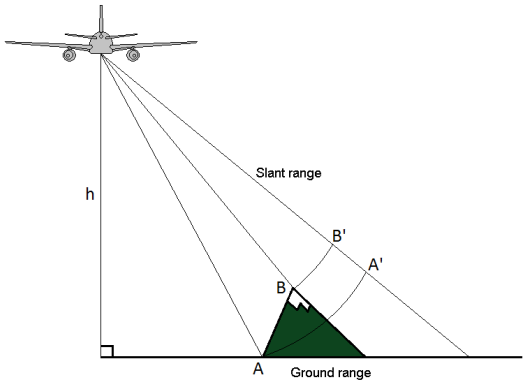

(a) Layover.

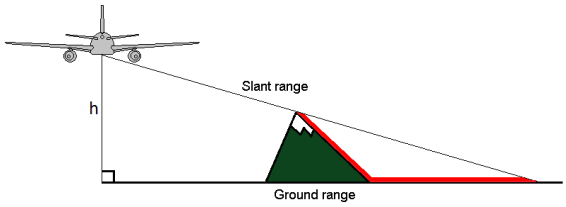

(b) Shadowing.

Figure 5.4: Layover and shadowing in side-looking geometry.

5.4 Flight

The system has been flown several times. The flight lines chosen can be seen in Figure 5.5. There are several calibration lines (UMass stadium area) and lines that fly over a variety of targets. Four corner reflectors equally spaced were placed on the field next to the stadium. The calibration flight lines were flown at different altitudes to get different look angles for the corner reflectors. The rest of the lines fly over rivers, ponds, fields, buildings, hills and forests. The altitudes for the first flight calibration

lines were 500 m, 1000 m and 2000 m. The rest of lines were flown at 500 m or 1000 m. The data processing has shown that flying at high altitudes, higher than 1200 m, makes the data processing not successful, resulting in not well focused images. Thus, the following flights were flown at altitudes between 600 m and 1200 m.

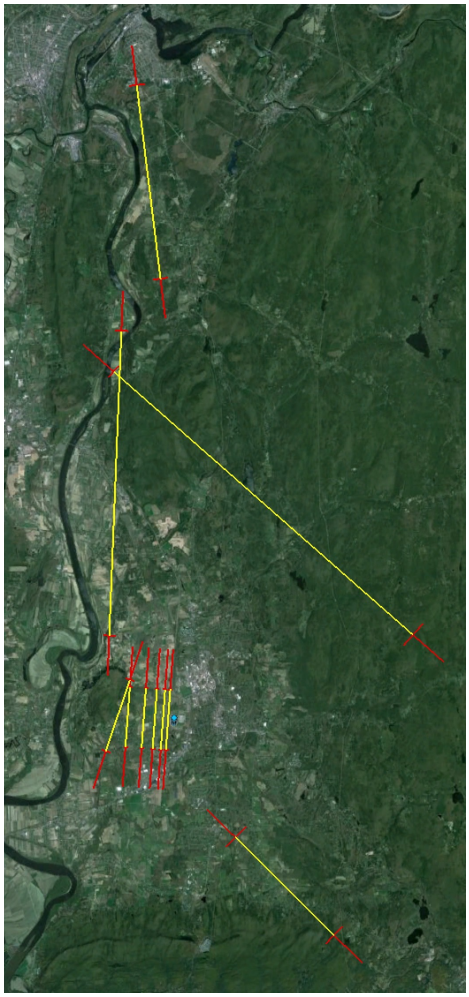

Figure 5.5: Flight lines for KaSI's first flight.

5.5 Data analysis

This section will discuss the data analysis done on one of the flight lines. The data was acquired on July 2016 over the area shown in Figure 5.6. The airplane was flying at 950 m, north to south with a right side-looking geometry. Both radars were

using HH polarization (i.e., horizontal both on transmit and receive). The data were processed using the backprojection time-domain algorithm described in [5].

Figure 5.6: Surface imaged by the dual-frequency system.

5.5.1 Qualitative data analysis

The SAR processed images for the first channel of each frequency band are shown in Figure 5.7. Notice that the images are processed in the slant range projection.

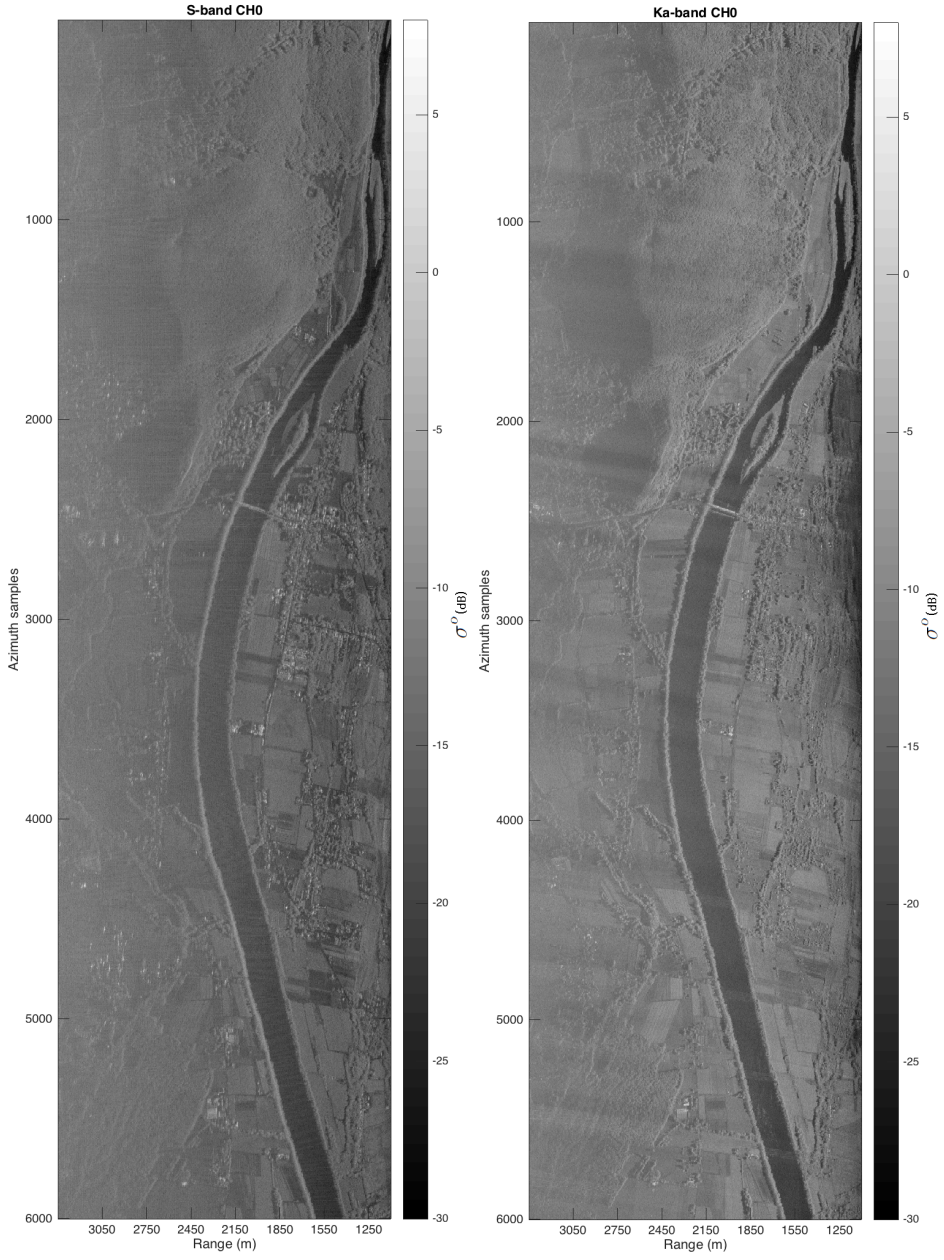

(a) SAR S-band image. (b) SAR Ka-band image.

Figure 5.7: SAR processed scenes for the dual-frequency system.

The processing works better in the medium range at both frequencies. The near range is unfocused at Ka-band. This is due to the insufficient knowledge of the motion data together with the narrow beam of the Ka-band antennas. Moreover, the scene contains stripes in the range direction that cause biases in the estimated backscattered power. At S-band, the far range is unfocused, visible on bright targets, due to the combination of inaccurate motion knowledge and big synthetic aperture. Hence, most of the analysis will focus on the medium range, ranging from 1300 m to 2500 m.

The first step to study the differences between the two bands is by taking the ratio between the first channels of both frequencies. Figure 5.8 shows the ratio, with red being Ka-band and cyan being the S-band. Notice the near range is dominated by cyan due to the unfocusing at Ka-band. At the far range, cyan dominates over red. This is due to the unfocusing at far range at S-band, which is worse than Ka-band, that adds noise to the image. The medium range area is mostly dominated by Ka-band, meaning that the normalized cross-section is higher than at S-band.

Figure 5.9 gives a close view to an area with fields. The focusing on the Ka-band image is poor at the near range, as it can be seen on bright targets. Differences in NRCS over different targets are expected since the wavelength at Ka-band is roughly ten times smaller than at S-band. Note that the contrast between certain type of fields is different at Ka-band and S-band.

The interferometric results for both S-band and Ka-band are shown in Figure 5.10. The dynamic range of the images has been changed to highlight height changes. The time-domain backprojection algorithm uses a DEM to estimate the phase-center of each pixel. Therefore, the heights resulting from the interferogram are referenced to the DEM and the heights associated to steep terrain (i.e, hills, mountains) are already included in the DEM. Hence, the terrain height does not affect the residual phase used to form the interferogram and only the height difference between the

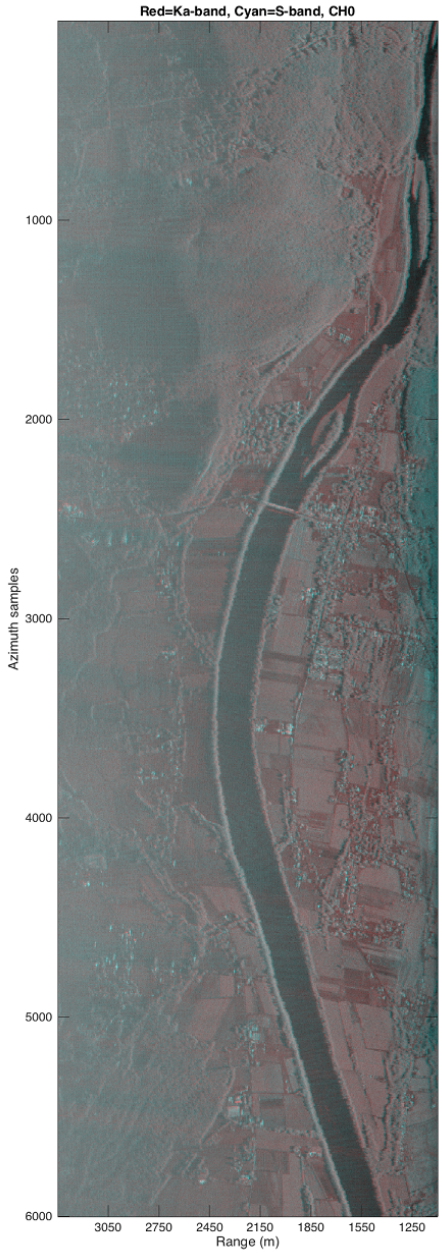

Figure 5.8: Ratio between Ka-band and S-band, first channel. The false color image uses red for Ka-band and cyan for S-band. If both frequencies matched perfectly, the image would be gray scale.

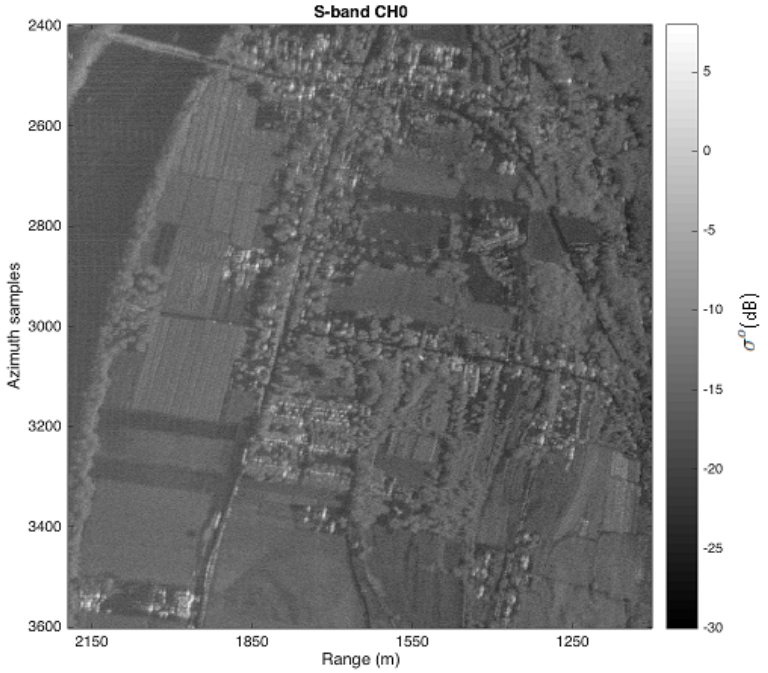

(a) Zoom in on the S-band image.

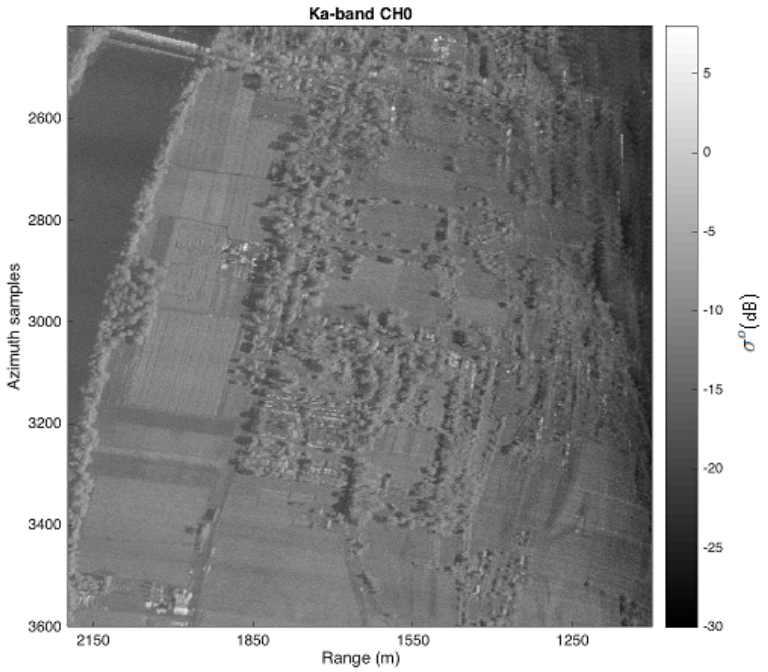

(b) Zoom in on the Ka-band image.

Figure 5.9: Close look of an area with different type of fields.

DEM and the resolution-cell's phase-center shows in the interferogram. For instance, mountains in both interferograms have similar height as the fields surrounding them. Processing and system artifacts are noticeable in the interferograms. Areas with noise will also appear with noisy phase (i.e., random phase). The radar backscatter over water should be low even at low look angles. Thus, the radar receiver's noise should dominate in ponds and rivers unless the look angles are close to nadir. While the river and shadows at Ka-band have random phase as expected, at S-band a phase ramp is present in the river and continues to the far range. Also, at Ka-band, the range stripes present in the SAR magnitude images show up in the interferograms causing bias in height. A close up of the interferograms, shown in Figure 5.11, gives more detail on the height differences between targets. For instance, these images show how trees have higher height values.

5.5.2 Radiometric calibration

The data have been calibrated in a simplistic sense by using statistics on radar backscatter from [4], which covers the radar cross-section statistics for a variety of targets (trees, crops, grass, soil, snow, roads) at a wide range of look angles (0 degrees up to 80 degrees). The calibration approach corrects the backscattered power to match the reference values obtained from [4]. In order for this correction to be considered a calibration, the correction applied to the backscattered power should be the calculated calibration constant of the system (measured using a target with known range and radar cross-section), instead of the values found on the literature. This is only an estimate based on experiments that can be biased due to, for example, the instrument setup, or ground conditions (i.e., soil moisture).

The radar response on trees has been identified as the best measure for calibrating the data presented here. The response of trees at both S-band and Ka-band does not strongly depend on the look angle. Thus, error in look angle estimation might be

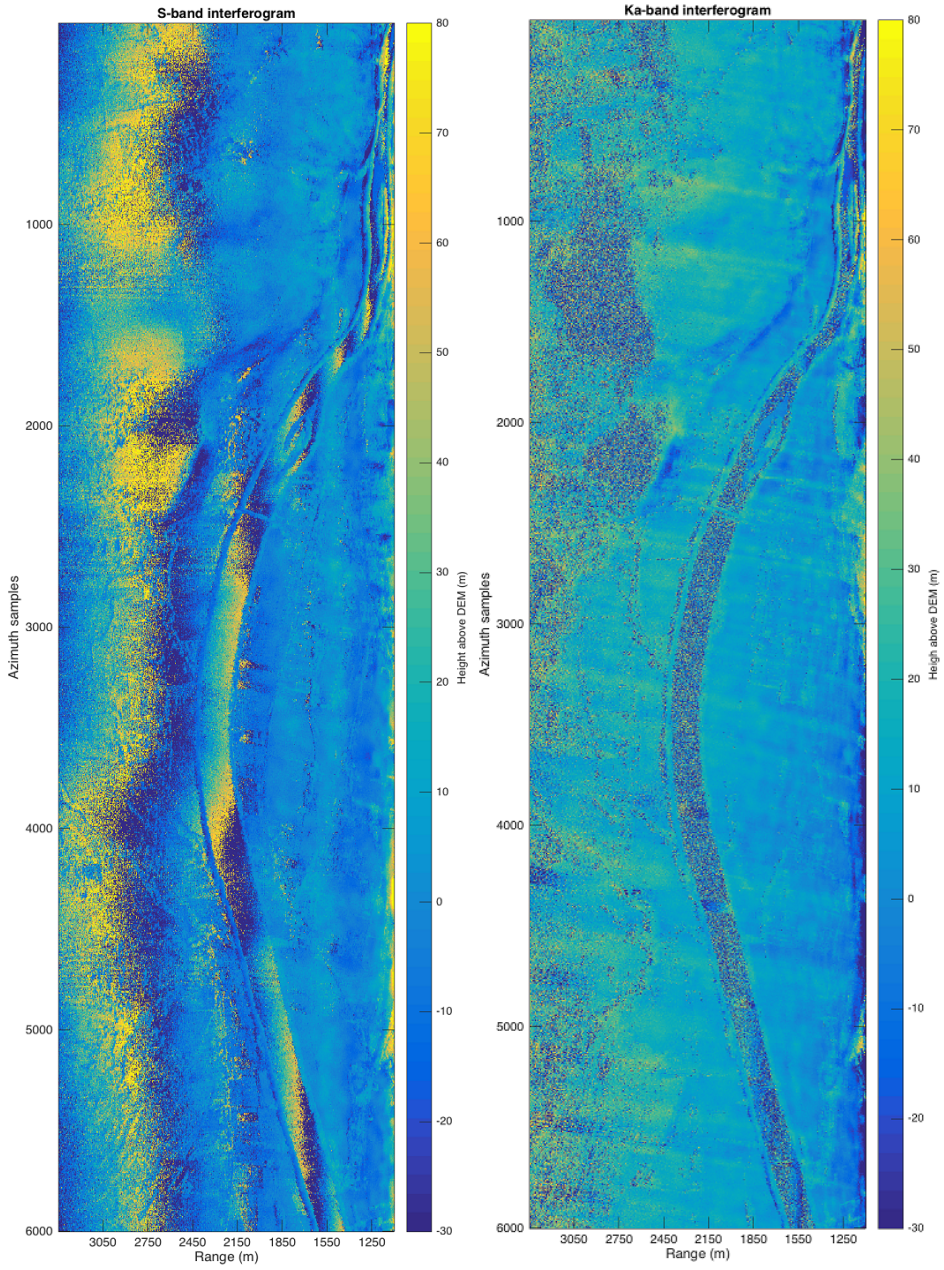

(a) S-band interferogram.

(b) Ka-band interferogram.

Figure 5.10: Interferometric scenes for the dual-frequency system.

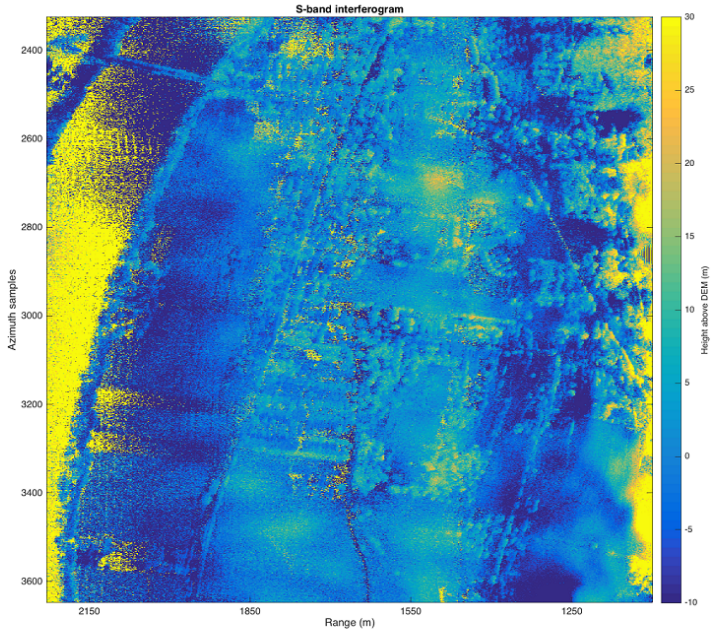

(a) Zoom in on the S-band interferogram.

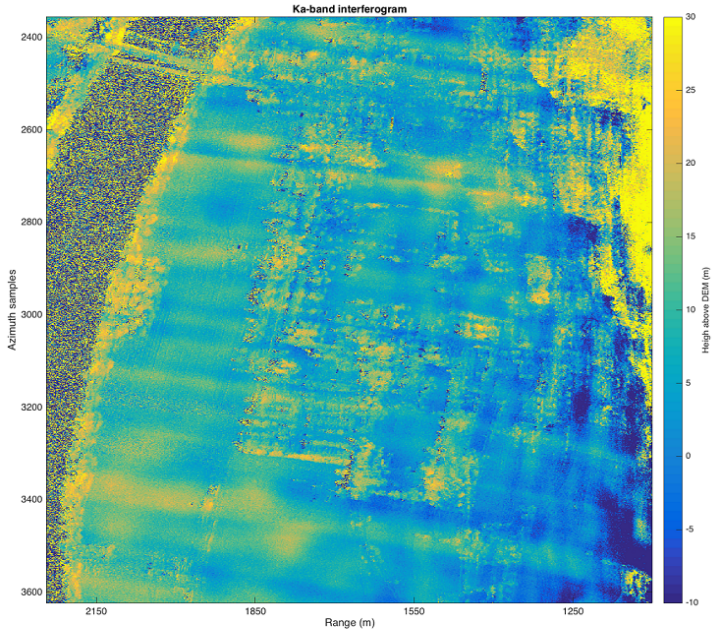

(b) Zoom in on the Ka-band interferogram.

Figure 5.11: Close look of an area with trees and different type of fields.

less of a concern when calibrating the data. Moreover, trees in this area are easier to identify compared to other targets, such as grass or crops, which can be hard to distinguish and determine properties such as height or roughness. Therefore, a forestry area is used in this calibration approach.

The estimation of the normalized radar cross-section is done by using the radar equation. Equation (4.7) in Section 4.8 is used to estimate the NRCS and get the calibration constant for the dual-frequency data. The correction for range is already done in the processing leaving the correction for the transmit power, P_t, area, A, and radar constant, K_r, to be determined. The transmit power is assumed to be a constant and is included inside the radar constant. The area is calculated for each pixel, taking into account the number of pulses per pixel, the azimuth resolution and the range resolution projected to ground coordinates:

$$A = \Delta r_{ground} \Delta az_{SAR} L = \frac{\Delta r}{sin\Theta} \Delta az_{SAR} L, \tag{5.1}$$

where Δr_{ground} is the ground projected range resolution, Δaz_{SAR} the azimuth SAR resolution, L the number of looks used to average (i.e., pulses averaged) and Θ is the look angle. Note that this calculation assumes a flat surface and does not take into account the slope of the terrain. However, the area of the image that this work discusses is mostly flat and therefore, this is a reasonable assumption.

The calibration constant can be calculated now by taking the mean value of backscattered power of a forestry area and applying the previously mentioned corrections:

$$K_r = \frac{P_{r_{forest}}}{P_{ref} A}, \tag{5.2}$$

where K_r is the calibration constant, $P_{r_{forest}}$ the uncorrected power over the forestry area and P_{ref} the reference value obtained from [4].

Target	σ_0(dB)		std(σ_0)(dB)	
	S	**Ka**	**S**	**Ka**
River 1	-26.8	-26.5	1.13	1.13
River 2	-16.48	-15.35	0.89	0.88
Shadow	-14.15	-13.21	0.91	1.03

Table 5.2: Noise equivalent sigma estimation.

With the calibration constant calibrated, the NRCS can be estimated as

$$\sigma^0 = \frac{P_r}{K_r A}. \tag{5.3}$$

5.5.3 Quantitative data analysis

This section presents the measured normalized radar cross-section for different targets in the processed images. Once a calibration constant is calculated for both frequencies, the data can be compared to existing datasets [4]. The results presented are meant to give a first overview on the main differences between S-band and Ka-band in terms of radar backscatter. However, not enough samples are used for the results to have any meaningful statistical value. Hence, further analysis of the collected and future datasets needs to account for different types of terrain, as well as a wider range of look angles.

The noise equivalent sigma can be estimated looking at the samples over water at high look angles or shadows. The mean and the standard deviation obtained for three different areas are shown in Table 5.2. The first samples were obtained on a portion of the river in the medium range. The second area of the river and the shadow samples fall in the far range and hence, the estimation is biased due to the noise added by the processing algorithm. Therefore, only the measurements over the river in the medium range are considered valid to estimate the noise equivalent sigma.

The normalized radar cross-section obtained for different targets is shown in Tables 5.3-5.8. Three to four samples, each one using the data of the two receivers, for each

target are used to estimate the mean value. The difference between these samples is usually not higher than 1 dB. The standard deviation of each individual sample is approximately 1 dB except for trees, where it is 2 dB. It is hard to compare the obtained values for different types of targets with the statistics found in [4] since different sources of error in both datasets are involved. First, the calibration can be considered good up to a few decibels. For instance, the values between the two channels of each radar usually differ between 0.20 dB and 1 dB. In some cases it is due to the slightly different viewing geometry between the two receive antennas while in others it can be explained by variations in gain in the receiver chains. Another source of error is the lack of ground truth data or similar target conditions on the measurements. The terms used in [4] to distinguish different targets do not describe well enough the distribution of targets, the roughness of the surface or the physical characteristics of targets at the time of the data acquisition. For instance, data of different crops such as corn, onions, beans or peas at different stages of growth fall under the same category. The optical data obtained in the flight is used to separate targets in different categories. The following lines compare the results for each of the targets with the values found in [4]:

- Crops. The sampled crops are estimated to be 2 meters high. The values at S-band for both datasets are similar within 1 dB. At Ka-band, KaSI measurements are 2 dB to 5 dB lower than the values found in the literature.

- Short crops. Short crops are shorter than the previous category. The values at S-band differ between 2 and 4 dB respect to the values of the literature. At Ka-band, the difference is 1.5 dB.

- Grass. The differences between datasets for this category are less than 1 dB at S-band and up to 2 dB at Ka-band.

Crops		σ_0(dB)	
		S	**Ka**
Look angle (deg)	**35-40**	-16.41	-12.3
	40-45	-15.9	-10.4
	45-50	-15.88	-10.58

Table 5.3: Normalized radar cross-section of crops.

Short crops		σ_0(dB)	
		S	**Ka**
Look angle (deg)	**40-45**	-14.52	-9.71
	55-60	-14.03	-8.69

Table 5.4: Normalized radar cross-section of short crops.

- Trees. The measurement of trees is consistent (less than 1 dB difference) for angles up to 45 degrees. At higher angles, the NRCS measured by KaSI is 5 dB higher at both S-band and Ka-band.

- Soil. The soil samples are consistent with the values found in the literature at both S-band and Ka-band with differences of 1-2 dB. However, one of the samples at S-band has an NRCS 3-4 dB higher than the two other similar samples (similar look angle and similar in the optical imagery). It might be explained by fluctuations in gain of the S-band radar during those pulses or an actual physical difference in the target imaged that cannot be sensed by Ka-band.

- Soil and grass. The values for this category are similar within 1.5 dB to the values found in the literature. Note that [4] does not have a specific category for this target. However, two separate categories (soil and grass) exist and the NRCS means for both categories differ in less than 1 dB.

The comparison between datasets shows differences in the NRCS measurements in crops both at S-band and Ka-band. The crops selected in this work are similar,

Grass		σ_0**(dB)**	
		S	**Ka**
Look angle (deg)	**40-45**	-16.10	-10.20
	49-51	-18.18	-12.55

Table 5.5: Normalized radar cross-section of grass.

Trees		σ_0**(dB)**	
		S	**Ka**
Look angle (deg)	**35-40**	-14.9	-12.67
	40-45	-15.02	-12.62
	45-50	-15.03	-11.34
	50-60	-13.55	-10.08

Table 5.6: Normalized radar cross-section of trees.

Soil		σ_0**(dB)**	
		S	**Ka**
Look angle (deg)	**41-43**	-16.50	-10.54
	44-46	-13.76	-10.39
	45-46	-17.88	-11.42
	61-62	-17.15	-12.05

Table 5.7: Normalized radar cross-section of soil.

Soil & grass		σ_0**(dB)**	
		S	**Ka**
Look angle (deg)	**47-50**	-18.45	-12.14

Table 5.8: Normalized radar cross-section of soil partially covered by grass.

which might explain why the results do not match the values found in the literature since the mean values used in [4] correspond to different types of crops. The values for trees are similar up to 50 degrees where the difference between datasets is 5 dB at both frequencies. This difference cannot be explained at the time of writing and further analysis should be done. Finally, the differences between datasets in NRCS for grass and soil at the two frequencies tend to be small. The results show that Ka-band and S-band have significant differences in terms of radar cross-section and hence, they can be used to better characterize or classify targets.

The quantitative analysis of the interferograms and the difference in height between frequencies present several challenges. As it is shown in Figure 5.12, the artifacts described in Section 5.5.1 are present when the height at Ka-band is subtracted from the height at S-band. Characterizing the height differences between frequencies is not feasible just by taking the difference between interferograms unless the system and the processing are improved. An alternative approach is to locally calculate the difference between a group of trees and the neighboring pixels associated to a field or a flat surface. This process is applied to both interferograms. Thus, the tree height at each frequency is estimated. The difference in height between frequencies is taken by subtracting the Ka-band height from the S-band height. If the areas sampled are chosen carefully, the bias introduced by the artifacts is reduced. The result of applying this method to different areas is shown in Figure 5.13. The mean value obtained for the difference in tree height between frequencies is 2.88 meters, which implies that Ka-band is slightly more sensitive to the upper tree structure while S-band penetrates more. However, more samples are needed to get a good estimate. Unfortunately, it is hard to find areas where the artifacts present in the data do not interfere with the estimations. Therefore, this result is just a starting point and further research needs to be done.

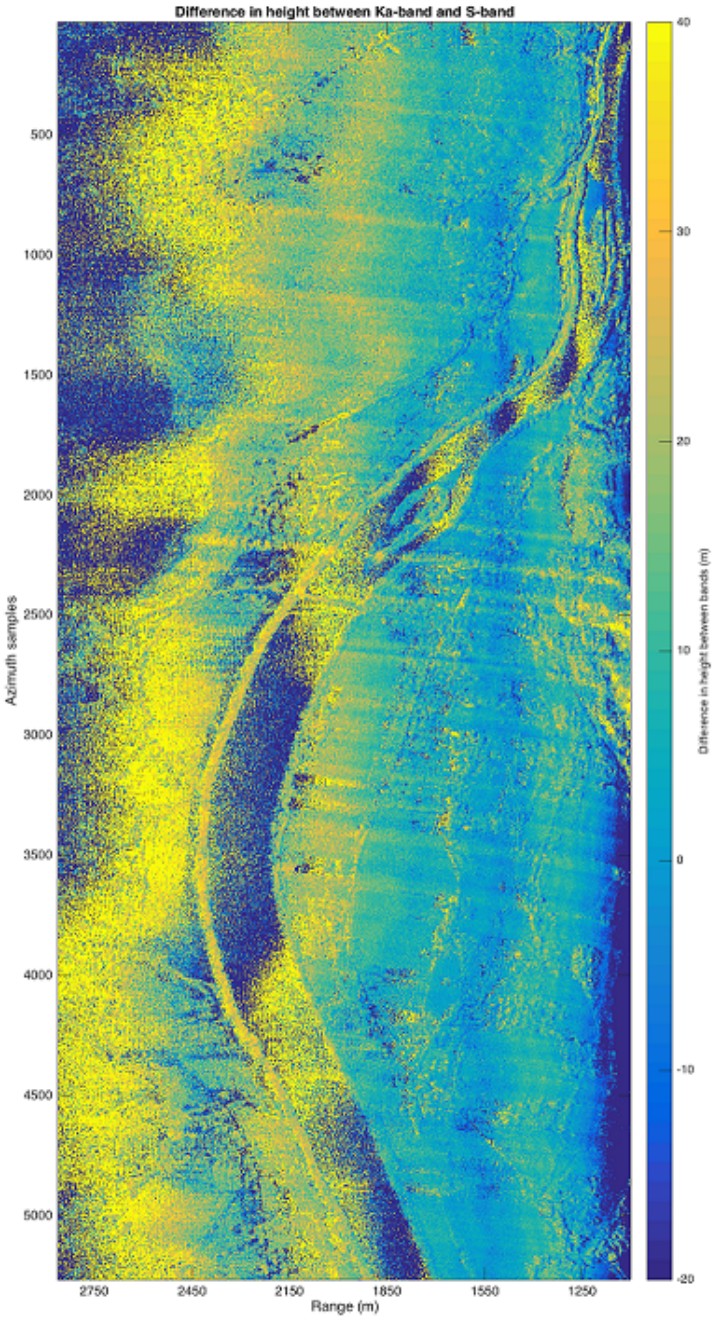

Figure 5.12: Height difference between frequencies.

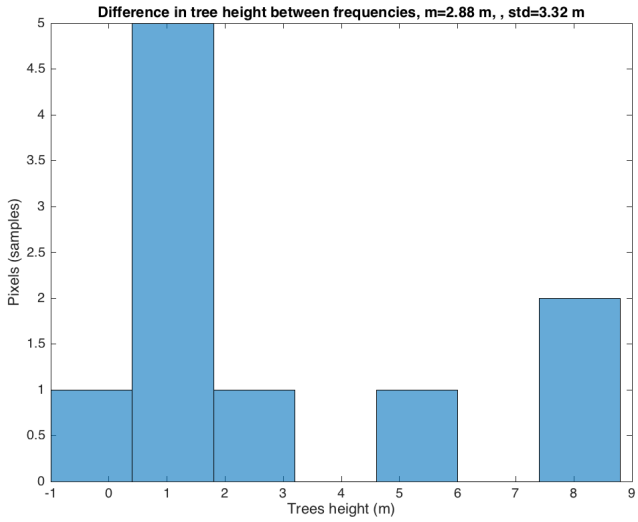

Figure 5.13: Tree height difference between frequencies.

CHAPTER 6

CONCLUSIONS

The work presented in this thesis has proven to be useful in measuring normalized radar-cross section of water and vegetation at Ka-band in a nadir-looking geometry. The scatterometer data match the observations found in the literature which opens possibilities for future data collections that will expand our knowledge on the radar Ka-band response. Moreover, these measurements are currently being used at the Jet Propulsion Laboratory and could potentially be used to design algorithms for the SWOT mission.

The working dual-frequency system is a unique instrument capable of producing valuable datasets. Although the data still needs to be explored more in depth, the first results have shown differences in both frequencies that can be exploited to better classify natural targets. Finally, even though more effort needs to be put in improving the interferograms, the work done is the first step towards the goal of estimating biomass and snow depth.

6.1 Contributions

The systems presented in this thesis are result of the work done in the last three years. The contributions of the author to the three different systems have been the following:

- S-band radar:
  - Designed and built the radar: transmitter, receiver, signal compression, LOs stage.

  - Built the power supply for the whole S-band system.
  - Integrated existing acquisition systems into the system.
  - Built the system to be deployed on ground acquisitions.
  - Adapted the system to be mounted on an airplane. Integrated the radar with GPS and IMU.
  - Tested the system on the ground.
  - Planned and successfully completed several flights.
  - Analyzed motion data and GPS data.
  - Coded the processing of real aperture radar images, for both ground and airborne experiments.
  - Continuously improved the radar (i.e., isolation antennas, dynamic range of the receiver), the supporting electronics and the setup on the airplane.

- Ka-band scatterometer:
  - Adapted the existing Ka-band radar to the scatterometer setup to meet the requirements of the project: temperature control and stability, receiver dynamic range...
  - Calibrated the system.
  - Completed several engineering and science collection flights.
  - Analyzed the motion and GPS data.
  - Processed the raw data from the calibration and the flights to get NRCS estimation and statistics.
  - Research done on tree height estimation.

- Dual-frequency system:

- Merged both the S-band and Ka-band radars into one system: common 10 MHz reference, signal generator...
- Designed a new antenna plate to mount the four receive antennas and the Ka-band transmit antenna taking into account coupling and shadowing of antennas as well as interferometric sensitivity.
- Completed engineering flights.
- Analyzed radar, GPS and motion data.
- Analyzed the processed SAR data and worked on interferometry.

6.2 Future work

This thesis covers three different systems. Each one of them has its own problems, challenges and applications. Future work can be done in any direction to improve any of the radars or the dual-frequency system. Therefore, the future work is here divided in the three systems:

- S-band radar:
  - Receiver characterization: Noise Figure, Dynamic Range, gain stability with temperature.
  - A temperature controller should be added for system stability.
  - When deploying on the airplane, weight and space need to be taken into account. Reducing the size and weight of the system might be a good idea: PCB design of the transceiver, lighter radar enclosure, lighter signal generator.
  - Calibration of the system. The system has been calibrated in ground and corner reflectors have been placed on the flight lines. New setups could be explored to get a better ground calibration. Calibration from the flight data still needs to be explored.

  - Characterization of the antennas.
  - Setup repeatibility. The system has been in constant evolution and so far, it has been hard to have a consistent setup.

- Ka-band scatterometer:
  - Ground calibration improvements. A new setup would help reduce the variane of the calibration.
  - Further study of the normalized radar cross-section of water, vegetation and other targets. Study of new water bodies will be necessary to have a better characterization of the response for different winds, water depth and water flow.
  - Synthetic aperture formation to improve the along-track resolution.
  - Further research on tree height estimation to measure biomass within the resolution-cell.
  - NRCS error budget.

- Dual-frequency system:
  - Reduce weight and volume.
  - Further analysis of SAR data.
  - Study NRCS differences between frequencies.
  - Further analysis of interferometry.
  - Study height differences between frequencies.

BIBLIOGRAPHY

[1] http://swot.jpl.nasa.gov. Surface Water and Ocean Topography Mission (SWOT) mission.

[2] http://nisar.jpl.nasa.gov. NASA ISRO Synthetic Aperture Radar mission, 2016.

[3] Duersch, Michael Israel. *Backprojection for Synthetic Aperture Radar*. PhD thesis, Brigham Young University - Provo, 2013.

[4] Fawwaz T. Ulaby, M. Craig Dobson. *Radar Scattering Statistics for Terrain*. Artech House, 1989.

[5] Lagoy, Dustin. Time domain SAR processing with GPUS for airborne platforms. Master's thesis, University of Massachusetts, 2017.

[6] Lei, Yang. *Electromagnetic Scattering Models for InSAR Correlation Measurements of Vegetation and Snow*. PhD thesis, University of Massachusetts, 2016.

[7] Rockwell B. Schrock. Integration and measurements of a ka-band interferometric radar in an airborne platform. Master's thesis, University of Massachusetts, 2012.

[8] Rodríguez, Ernesto. Surface Water and Ocean Topography Mission (SWOT) Project. Science Requirements Document. Tech. rep., NASA Jet Propulsion Laboratory, 2016.

[9] Vandemark, D., Chapron, B., Sun, J., Crescenti, G. H., and Graber, H. C. Ocean Wave Slope Observations Using Radar Backscatter and Laser Altimeters. *Journal of Physical Oceanography 34*, 12 (2004), 2825–2842.

[10] Vedantham, H. Design and Development of TIMMi, An Interferometric Radar. Master's thesis, University of Massachusetts, 2008.